Solid State Spectroscopy II
— XAFS, PES —

(BL1A, 5A, 5B, 6A2, 7A, 8B1, 8B2)

(BL-7A)

Structural Analysis of Amorphous Al_2O_3-Y_2O_3 Films

Naoshi OZAWA[1], Takeshi YAO[1] and Teiichi HANADA[2]

[1] *Graduate School of Energy Science, Kyoto University, Kyoto, 606-8501 Japan*

[2] *Graduate School of Human and Environmental Studies, Kyoto University, Kyoto, 606-8501 Japan*

Among rare earth oxides, Y_2O_3 has higher melting point than that of Al_2O_3 and is applied for a laser crystal and a heat-resisting material. Y_2O_3 is also used as a mother material for producing tri-valence rare earth ion phosphor and the applications for an optical waveguide and a thin film luminescent material have been reported. In this study, the structure of Al_2O_3-Y_2O_3 amorphous films were analyzed from Al-K XANES and Y-K_{III} XANES spectra. Samples were synthesized by means of rf-spattering, a method by which amorphous material can be easily obtained from material with high melting point.

Al_2O_3-Y_2O_3 amorphous film samples with Y_2O_3 content from 9 to 82 % were prepared. X-ray absorption was measured by BL-7A at UVSOR, Institute for Molecular Science, Okazaki, Japan. The storage ring was operating at electron energy of 750 MeV. The spectra were collected in a total electron yield mode at room temperature by an electron multiplier, using $KTiPO_4$ (KTP) (011) double crystal monochromator.

Figure 1 shows Al-K XANES spectra of the samples. $AlPO_4$ and Al_2O_3 were used as references of Al with coordination number (CN) 4 and 6, respectively. The peak intensity at about 1566 eV decreased with the increase of Y_2O_3 content. It is considered that the decrease of Al with CN 4 is indicated. Figure 2 shows Y-L_{III} XANES spectra of the samples. Spectra of Y_2O_3 and $LaYO_3$ are shown as a reference of Y with CN 6 and spectrum of YVO_4 is shown as a reference of Y with CN 8. The Y-L_{III} XANES spectra of the samples were almost unchanged with the Y_2O_3 content and were similar to that of YVO_4. This indicates that CN of Y in Al_2O_3-Y_2O_3 amorphous films is 8, regardless of the Y_2O_3 content.

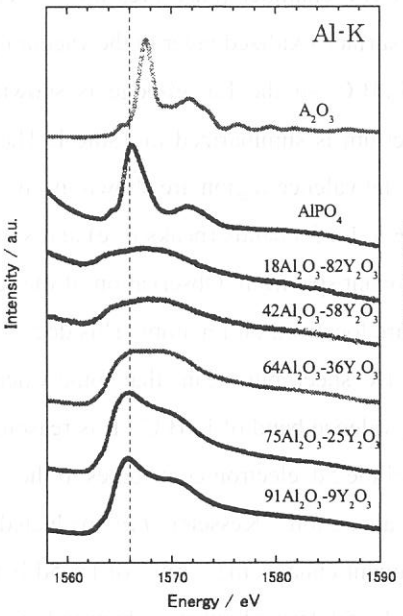

Fig.1 Al-K XANES spectra of Al_2O_3-Y_2O_3 amorphous films

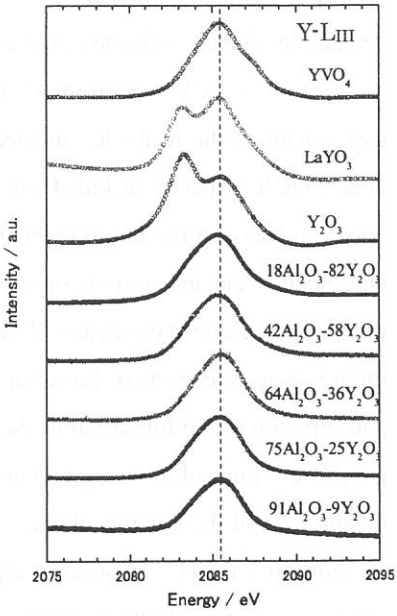

Fig.2 Y-L_{III} XANES spectra of Al_2O_3-Y_2O_3 amorphous films

(BL1A)

La 3d-edge Photoabsorption and Resonant Photoelectron Spectroscopy of Rare-earth Borocarbide LaB_2C_2

Hiroshi Oji,[a] Shinji Hasegawa,[a] Kazuya Suzuki,[b] and Nobuhiro Kosugi[a]

[a]*Institute for molecular Science, Myodaiji, Okazaki 444-8585, JAPAN*

[b]*Graduate School of Engineering, Yokohama National University, Hodogawa-ku, Yokohama 240-8501, JAPAN*

In rare-earth borocarbides RB_2C_2 (R: rare-earth (RE) metals) rare-earth metal cations are intercalated in the planar BC sheets. These intercalation compounds show interesting electronic and magnetic properties, such as superconducting behavior (T_c=2.4K for LuB_2C_2[1]). Therefore, it is important to know their electronic structure in order to clarify the mechanism of these properties. In the present study, the La 3d X-ray absorption spectroscopy (XAS) and valence-band resonant photoelectron spectroscopy (RPES) were used to reveal the partial density of states at the core-excited atom for lanthanum borocarbide (LaB_2C_2). Use of the relatively high energy photons of BL1A at the UVSOR facility (hν~830eV) allows us to perform the bulk-sensitive measurement.

The measurement of X-ray absorption and photoelectron spectra was performed at the BL1A soft X-ray beamline equipped with the double crystal monochromator. A pair of beryl ($10\bar{1}0$) crystal was used as a monochromator crystal, where the bandpass of monochromatized light was 0.6eV around 850eV. The XAS spectra were measured by the total electron yield mode. A SCIENTA SES-200 hemispherical electron energy analyzer was used for the measurement of RPES spectra. The energy resolution of the analyzer was set to be ~0.4eV and the total energy resolution for the measurements of the photoelectron spectra was ~0.7eV. The intensity of the spectra was normalized by the mesh yield (I_0). A polycrystalline flake of LaB_2C_2 cleaved in the atmosphere was introduced in the UHV chamber (base pressure: $<3X10^{-10}$Torr), and the sample surface was scraped by diamond files to remove surface oxidized layer in the vacuum just before the experiment.

The XAS spectrum of LaB_2C_2 in the La 3d-edge is shown in Fig. 1. According to Ref. 2, the assignment of the peaks in the spectrum is summarized in Table I. The off- (hν=826.4eV) and on- (834.3eV, peak 2) RPES spectra of LaB_2C_2 in the valence region are shown in Fig. 2. Abscissa corresponds to the binding energy relative to the Fermi level (E_F). La 5p bands (peaks d, e) and some bands near to the E_F (peaks a-c) are significantly enhanced in the on-resonant spectrum. Observation of the resonance effect on the valence suggests that some valence states near to E_F are localized on La atom. This does not support the complete donation of the three valence electrons of La to the BC sheet, but means that some valence (5d or 6s) electrons of La atom are participating to the formation of the valence band of LaB_2C_2. It is reasonable to expect that the $6s^2$ electrons are completely ionized in the system and the $5d^1$ electron contributes to the valence band. This is in agreement with the analysis of the theoretical band calculation.[3] Kesseler *et al.* evaluated the number of electrons localized on a La atom in a La@C_{82}, from the resonant enhancement ratio of La 5d band to that of La 5p. According to their scheme, we estimated the number of La 5d derived-valence electron localized on a La atom in LaB_2C_2 roughly to be 0.3.

References

1) J. van Duijn et al, *Phys. Rev.* **B62** (2000) 6410.

2) B. T. Thole et al. *Phys. Rev.* **B32** (1985) 5107.

3) H. Harima and M. Shirai, *J. Phys. Soc.* submitted.

4) B. Kessler et al, *Phys, Rev. Lett*, **76** (1999) 2289.

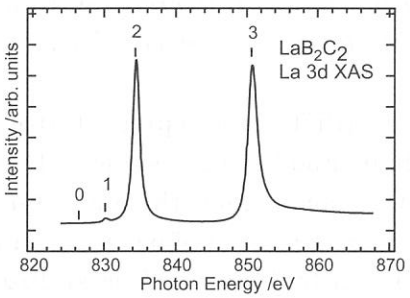

Fig. 1. La 3d-edge XAS spectrum of LaB_2C_2.

TABLE I. The assignment of the peaks in the XAS spectrum of LaB_2C_2.

Peak#	Peak Pos. /eV	Assignments
1	830.2	La $3d_{5/2}$ -> 4f ($^3D_1$)
2	834.3	La $3d_{5/2}$ -> 4f ($^3P_1$)
3	850.6	La $3d_{3/2}$ -> 4f ($^1P_1$)

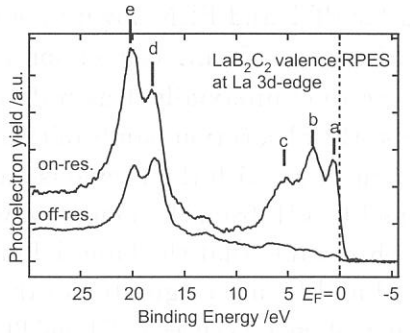

Fig. 2. Off- and on-resonant valence-band PES spectra of LaB_2C_2.

(BL-1B)

Anisotropic Absorption Spectra of Polyester Films due to Valence Electrons in Shallow and Deep Levels

Isuke OUCHI, Ikuo NAKAI[A] and Masao KAMADA[B]*

Faculty of Engineering, Tokushima Bunri University, Shido, Kagawa 769-2193
[A]*Faculty of Engineering, Tottori University, Koyama, Tottori 680-8552*
[B]*UVSOR, Institute for Molecular Science, Myodaiji, Okazaki 444-8585*

Polyethylene terephthalate (PET) is a representative aromatic polyester having a benzene ring in the main chain, and has been subject of study by many researchers with different interests, since long ago. Polyethylene 2,6-naphthalate (PEN) is similar polyester with a naphthalene ring instead of benzene. Both polymers can be extruded in sheet form, and, after biaxially drawn and crystallized, are utilized for variety of applications. Their optical and photo-physical properties have also been pursued. Absorption spectra of PET films in visible and ultraviolet regions manifest three bands between 300 and 190 nm; their nature was examined in detail, particularly for the first band at 300 nm.[1] The third band at 197 nm was found to consist of two peaks of different polarization by a molecular orbital calculation using π electron approximation, whereas it was not certain from experiments which of the two peaks had parallel polarization, because of the limit of the measurement in air or nitrogen.[1]

We have been trying to investigate the deep levels of valence electrons in oriented polyester films for the past years. At the present, optical constants and absorption spectra have been obtained for PET and PEN down to 50nm, or up to 24.7eV, from the reflection spectra by use of Kramers-Kronig conversion and Fresnel Formula. Fig. 1 illustrates the absorption spectra of uniaxially drawn PET and PEN films as a function of photon energy. Table I list the absorption bands of these films in relation to the peak position and polarization, comparing with the previous data obtained in air; absorption bands therein are denoted as I to VII, from the longer wavelength to the shorter.

If magnified, it is clearly observable that the band III of PET consists of two peaks as listed in Table I. Bands I, II and III are originated in the allowed $^1A_g \rightarrow {}^1B_u$ transitions due to $\pi \rightarrow \pi^*$ excitation; major difference between PET and PEN appears in this region.

The rest of the region, consisting of Bands IV to VII, resembles each other in spectral shape and peak positions, although there are minor differences in the polarization and shape. These bands must be caused by the transitions associated with σ electrons. The number of valence σ electrons in a repeat unit of PET and PEN are 54 and 68, respectively; the ratio of these numbers must be equal to the ratio of the integrated area of the peaks of each polymer, if taken for isotropic samples. The peak area is larger for PEN than PET, but not in proportion to 68 vs. 54, because of the anisotropy of the sample and mostly of the inevitable error caused by the method of approximation in the calculation of Kramers-Kronig conversion.

The feature in the region near Bands VI and VII resembles that for other polymers

---

● Present address: Saga University

such as polystyrene and PMMA as recorded by electron energy loss spectroscopy many years ago[2,3]. This may be understandable from the fact that a majority part of most polymers consists of carbon and hydrogen atoms.

	PET				PEN			
Band No.	absorption peak	polarity	previous data*		absorption peak	polarity	previous data**	
	A (eV)		exp.	calc.	A (eV)		exp.	cal.
VII	800 (15.5) vvs	∥			800 (15.5) vvs	∥		
VI	930 (13.3) vs	∥			920 (13.5) vs	∥		
V	1100 (11.3) sh	⊥			1100 (11.3) sh	⊥		
	1200 (10.3) sh	∥			1230 (10.3) sh	∥		
IV	1480 (8.4) sh	⊥			1550 (8.0) sh	∥		
					1700 (7.3) sh	⊥		
								n.a.
III	1860 (6.7) vs	∥	(6.29)	(6.44)	2200 (5.6) vs	∥		
	1970 (6.3) vs	⊥		(6.33)	2400 (5.2) vvs	∥	(5.5)	
					2500 (5.0) sh	∥	(4.8)	
II	2420 (5.1) vs	∥	(5.09)	(5.27)	2780 (4.5) sh	∥		
	2500 (5.0) vs	∥			2880 (4.3) s	∥	(4.2)	
					2990 (4.1) sh	∥	(4.0)	
I	2800 (4.4) sh	⊥			3260 (3.8) sh	∥		
	2900 (4.3) w	⊥	(4.26)	(4.66)	3410 (3.6) w	∥	(3.7)	
	3000 (4.1) w	⊥	(4.13)		3580 (3.5) w	∥	(3.5)	

Table 1. **Absorption peaks of PET and PEN films**
Peak intensity is denoted by the abbreviation; vvs=extremely strong, vs=very strong, s=strong, w:=weak, sh= shoulder. Also, * designates the reference [1]; ** [3].

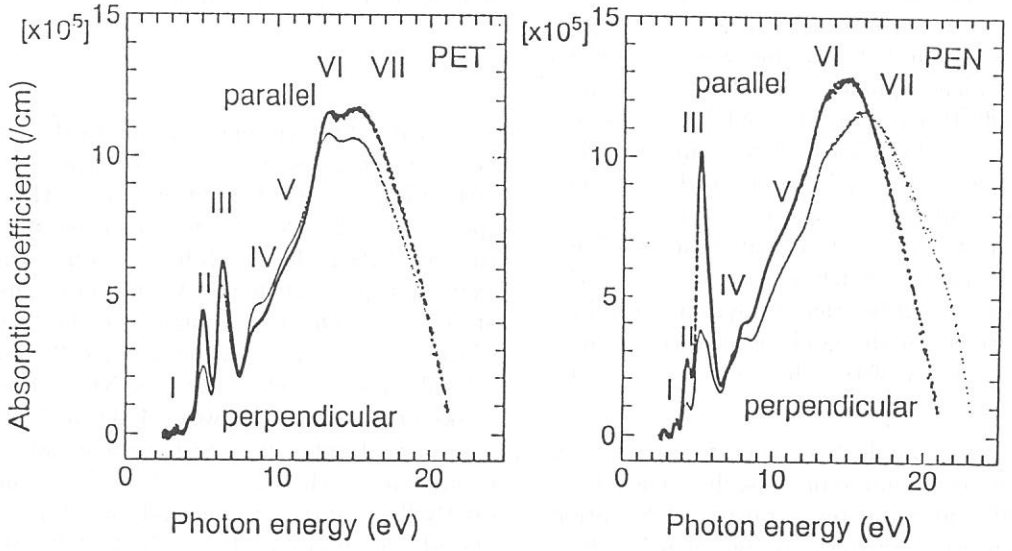

1) I. Ouchi, Polym. J., 15 (1983) 225.
2) T. Inagaki, E.T. Arakawa, R.N. Ham,M.W. Williams, Phys Rev., B15 (1977)3243.
3) J.Jritsko and R.W. Bigelow, J. Chem. Phys. 69 (1978) 4162.

(BL 2B1)

Orientation of Ammonia on ZnO(10$\bar{1}$0)

K.Ozawa, T. Hasegawa, K. Edamoto, K. Takahashi* and M. Kamada*

Department of Chemistry, Tokyo Institute of Technology, Ookayama, Meguro-ku, Tokyo 152, Japan
**Institute for Molecular Science, Myodaiji, Okazaki 444-8585*

The orientation of ammonia (NH_3) adsorbed on the ZnO(10$\bar{1}$0) surface at room temperature has been investigated by near-edge X-ray absorption fine structure (NEXAFS) spectroscopy. The NEXAFS technique is a well established method to determine the orientation of a wide variety of adsorbed species on the surfaces [1]. However, no such attempt has been made so far for adsorbed ammonia, partly because the NEXAFS spectra of adsorbed NH_3 show only broad resonance features with a poor dependence on the electric vector of the light [2]. Regarding adsorbed ammonia, therefore, electron stimulated desorption ion angular distribution (ESDIAD), photoelectron diffraction (PhD), and X-ray emission spectroscopy (XES), etc., have been used to investigate the orientation of adsorbed NH_3. The present study demonstrates that the polarization dependent NEXAFS measurements combined with curve fitting analysis are also capable to determine the orientation of adsorbed NH_3

The N K-edge NEXAFS spectra were measured at beam line 2B1 with the N KLL Auger electron yield mode with a constant final state energy of 375 eV. The ZnO(10$\bar{1}$0) sample was oriented so that the incidence plane of the light was parallel to the [000$\bar{1}$] azimuth. The NEXAFS spectra were normalized by photon flux estimated from the photocurrent of a gold mesh at the entrance of the UHV chamber. The photon energy was calibrated using the absorption feature at 284.5 eV in the photocurrent, which is associated with the π^* resonance of highly oriented pyrolitic graphite (HOPG) formed on the gold mesh as a contaminant. The accuracy of the photon energy is $\pm$ 0.5 eV.

Our recent photoelectron spectroscopy study has revealed that ammonia adsorbs molecularly on ZnO(10$\bar{1}$0) at room temperature. Adsorption reaches saturation at the coverage of 0.5 (3.0×10^{14} cm^{-2}). Fig. 1 shows a series of the N K-edge NEXAFS spectra from the NH_3-saturated ZnO(10$\bar{1}$0) surface as a function of the incidence angle of the light θ_i relative to the surface normal. All the NEXAFS spectra do not exhibit a sharp resonance as is often observed for the adsorbates with the π conjugated system [1]. However, at least three resonances are resolved at $\sim$ 401, 404 and 407 eV (indicated by bars in the bottom spectrum). The N-K edge excitation spectra for the free NH_3 molecule [3] have shown a threshold excitation peak at 400.6 eV and an intense peak at 402.3 eV, which are assigned to the transitions of the N 1s electrons to the $4a_1$ and 2e molecular orbitals, respectively. For free NH_3, three more peaks are observed between 402.8 and 404.2 eV with a weak intensities and are associated to the transitions to the N $3p_z$ (a_1), 4s (a_1), and $4p_{x,y}$ (e) Rydberg states, respectively [3]. Since ammonia adsorbs molecularly on ZnO(10$\bar{1}$0), the excitation features found in free NH_3 should be also observed in the adsorption system, although the position and the width of the peaks as well as the intensity ratio of the peaks are considered to be modified because of the bonding interaction of the molecular orbitals of NH_3 with the substrate or-

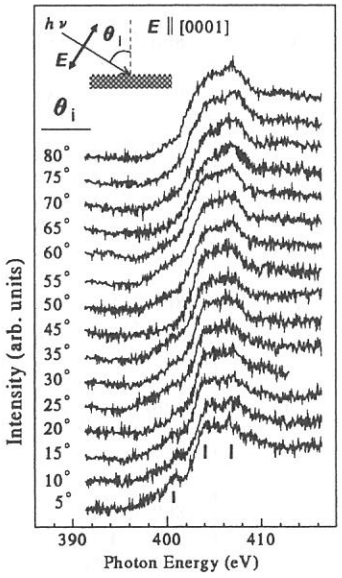

Fig. 1. The N K-edge NEXAFS spectra at various incidence angle θ_i of the light. The angle is measured from the surface normal direction. The incidence plane of the linearly polarized light is parallel to the [000$\bar{1}$] azimuth.

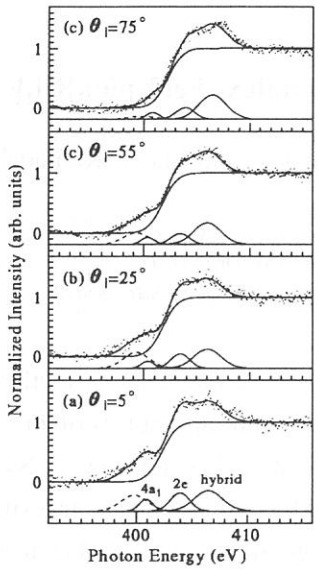

Fig. 2. The results of curve fitting analysis for the NEXAFS spectra. Four Gaussian functions for the resonance features and an error function for the continuum step are assumed. The line through the dots are the best fitted results.

bitals [2]. We, therefore, interpret the peaks at 401 and 404 eV as the excitations of the N 1s electron to the $4a_1$ and 2e orbitals of adsorbed NH_3, respectively. The third peak at 407 eV can be related to the excitation to the hybrid Rydberg states formed between the N $3p_z$ and N 4sp orbitals of NH_3 and the substrate Zn 4sp orbitals.

Fig. 1 shows that the observed peaks at 401, 404 and 407 eV exhibit a rather weak, but an obvious polarization dependence. In order to quantify the polarization dependence of these peaks, the NEXAFS spectra were decomposed by the curve fitting procedure using Gaussian functions for the peaks and an error function for the continuum step [1]. A selected set of the result is shown in Fig. 2. Apart from the peaks at 401, 404 and 407 eV, which are related to the $4a_1$, 2e and hybrid Rydberg states, respectively, another peak (shown by dashed line) is requisite to reproduce the low energy tail. The origin of this peak for the present system is unclear, but the NH_3 $3a_1$–Zn 4sp antibonding state could be responsible for the low energy tail.

Because of the large overlap between the $4a_1$ peak and the low excitation energy peak (dashed line), the intensity of these peaks seems to be correlated each other, especially at large θ_i where the $4a_1$ peak becomes a shoulder. Thus, the polarization dependence of the 4 a_1 peak intensity is ambiguous. On the other hand, the 2e and the hybrid peaks, which are well separated from the $4a_1$ and low excitation energy peaks, shows a clear polarization dependence.

Fig. 3 shows the θ_i dependent change in the

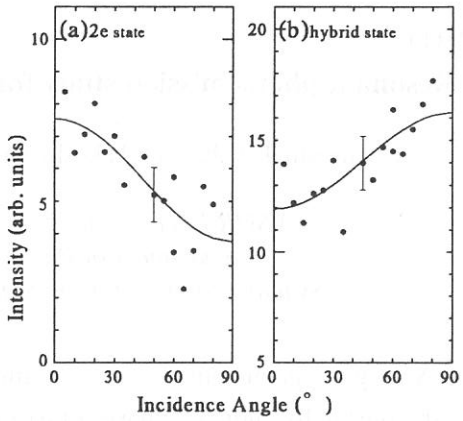

Fig. 3. The θ_i dependence of the intensities of the peaks, which are associated with (a) the 2e state and (b) the hybrid Rydberg state. Filled circles are the observed data. The solid lines are the best fit to the data using Eqs. 9a and 10a in Ref. [4].

peak intensities of these peaks. The 2e peak exhibits a decreasing trend with increasing θ_i. The 2e molecular orbitals are mainly composed of the N $3p_{xy}$ orbitals (the z axis is taken along the C_{3v} molecular axis). If NH_3 adsorbs with the C_{3v} axis tilted in the $[000\bar{1}]$ azimuth, the dependence of the 2e peak intensity on the incidence angle of light θ_i is expressed by Eq. 9a in Ref. [4]. The best fit to the data points is obtained at the molecular tilt of 33 ± 5° from the surface normal. On the other hand, the the peak associated with the hybrid states at 407 eV shows an increasing trend with increasing θ_i (Fig. 3b). This result implies that the molecular orbitals with the different symmetry from the 2e symmetry should be contribute significantly to the 407-eV peak. Namely, the Rydberg orbitals with the a_1 symmetry is responsible for the observed θ_i dependence. In such a case, the the θ_i dependent peak intensity can be fitted using Eq. 10a in Ref. [4] with the tilt angle of 41 ± 5°. Analysis of the intensity variation of these two resonances concordantly indicates that molecularly adsorbed ammonia on $ZnO(10\bar{1}0)$ is inclined in the $[000\bar{1}]$ azimuth.

References

[1] D.A. Outka and J. Stöhr, J. Chem. Phys. *88* (1988) 3539.

[2] J. Hasselström et al., J. Chem. Phys. *110* (1999) 4880.

[3] J. Schirmer et al., Phys. Rev. A *47* (1993) 1136.

[4] J. Stöhr and D.A. Outka, Phys. Rev. B *36* (1987) 7891.

(BL2B1)

Resonant photoemission study for spin-crossover complex $[Fe(2\text{-}pic)_3]Cl_2EtOH$

Kazutoshi Takahashi[A], Takeshi Tayagaki[B], Koichiro Tanaka[B], and Masao Kamada[C]

[A] *UVSOR Facility, Institute for Molecular Science, Okazaki 444-8585*
[B] *Department of Physics, Kyoto University, Kyoto 606-8502*
[C] *Synchrotron Light Application Center, Saga University, Saga 840-8502*

An organometal spin-crossover complex $[Fe(2\text{-}pic)_3]Cl_2EtOH$ (2-pic=2-aminomethyl-pyridine) shows the thermally-induced phase transition of two stages at critical temperatures of 114 and 121 K [1]. The high- and low-temperature phases correspond to the high-spin (HS) phase with S=2 and low-spin (LS) phase with S=0, respectively. In addition to the thermally-induced phase transition, $[Fe(2\text{-}pic)_3]Cl_2EtOH$ shows the dramatic change in chromic and magnetic properties due to the photo-induced phase transition, when it is excited by photons at low temperatures. Up to now, these thermally- and photo-induced phase transitions in $[Fe(2\text{-}pic)_3]Cl_2EtOH$ have been investigated mainly by optical and magnetic methods, but to our knowledge, there are a few works that highlight the electronic structure in the wider energy range [2]. In order to clarify the photo-induced phase transitions, it is also indispensable to understand the electronic structure in the wider energy range. In this study, we have carried out a resonant photoemission study at N 1s-2p and Fe 2p-3d excitation regions for $[Fe(2\text{-}pic)_3]Cl_2EtOH$.

Experiments have been carried out at the beam line BL2B1 in the UVSOR facility. Powder samples of $[Fe(2\text{-}pic)_3]Cl_2EtOH$ were synthesized at Kyoto university. The sample was attached on the sample holder using a carbon adhesive tape and introduced to measurement chamber without being exposed to air using a glove-bag filled with nitrogen gas and a load-lock chamber. The sample temperature was changed between 300 and 100 K using liquid nitrogen. The sample was irradiated by visible light from the Ar^+-ion laser of about 9 mW in multi-line mode at 100 K in order to cause the photo-induced phase transition. Photoemission spectra were measured using a double-pass CMA analyzer. Total energy resolution is about 1.5 eV for N 1s-2p excitation region.

Figure 1 shows the photoabsorption spectrum at the Fe $2p_{1/2}$ and $2p_{3/2}$ edges of $[Fe(2\text{-}pic)_3]Cl_2EtOH$ at HS phase. Figure 2 shows the difference spectra in valence band and Fe 3p regions at the Fe $2p_{1/2}$ and $2p_{3/2}$ edges of $[Fe(2\text{-}pic)_3]Cl_2EtOH$ at HS phase. Off-resonance spectrum (A) is also shown in Fig. 2. The features at 688 and 635 eV in kinetic energy correspond to the L_3VV and $L_3M_{23}V$ Auger lines, respectively. As shown in Fig. 2, spectral intensities of these features increase at Fe $2p_{2/3}$ edge. It is also found that the photoemission intensity of valence-band (feature 1) and satellite of Fe 3p (feature 3) increase at Fe $2p_{1/2}$ edge. Figure 3 shows the photoabsorption spectrum at the N 1s edge. The feature at 399 eV corresponds to the π^* resonance. On the other hand, the features at 406, 407.5, and 416 eV correspond to σ^* resonances. Figure 4 shows the difference spectra in valence-band and Fe 3p regions at the N 1s edge of $[Fe(2\text{-}pic)_3]Cl_2EtOH$ at HS phase. Off-resonance spectrum (A) is also shown in Fig. 4. The main features in the difference spectra correspond N KVV Auger lines. As shown in Fig. 4, it is found that the kinetic energy of the KVV Auger lines shift to lower kinetic energies with increasing the excitation energy from π^* resonance to σ^* resonance regions. In contrast with the Fe $L_{2,3}$ excitation region, it is found that the spectral intensity at valence-band and Fe 3p regions show almost no change at N K excitation region.

We have also measured photoabsorption and photoemission spectra for LS and photo-induced (PI) phases. It is found that the feature at 416 eV in the absorption spectrum at N K edge region broaden at LS phase and the energy separation of features around 407 eV increase at PI phase. It is considered that these spectral changes are indicative of the change in Fe-N bonding at thermally- and photo-induced phase transitions. However, we could not find electronic structure changes in resonant photoemission spectra at LS and PI phase with finite energy resolution in this study. Further investigations with higher energy resolution are in progress.

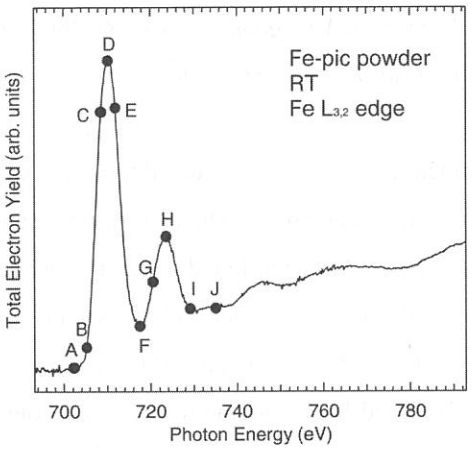

Figure 1. Photoabsorption spectrum at Fe $2p_{1/2}$ and $2p_{3/2}$ edges for high-spin phase.

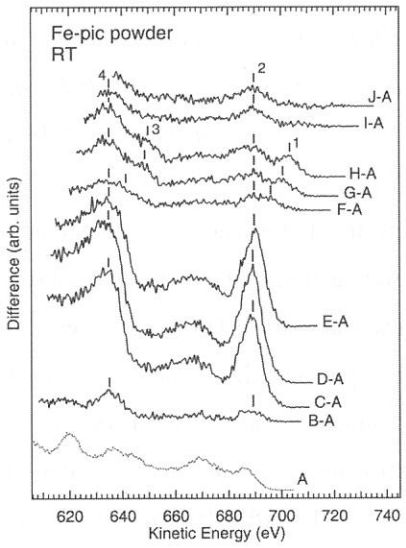

Figure 2. Difference photoemission spectra at Fe $2p_{1/2}$ and $2p_{3/2}$ edges for high-spin phase.

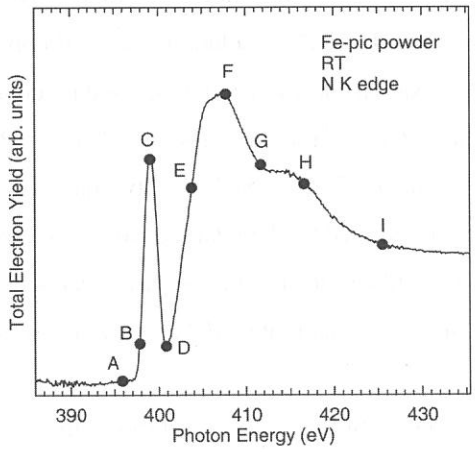

Figure 3. Photoabsorption spectrum at N 1s edge for high-spin phase.

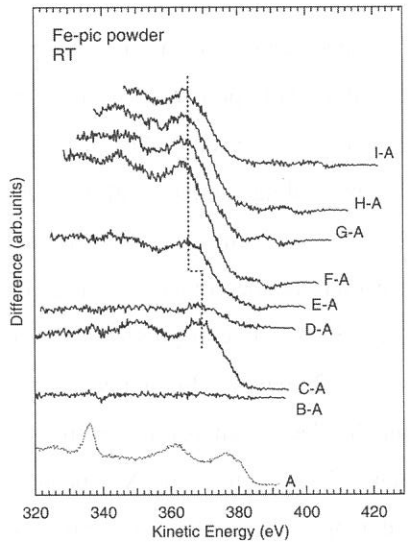

Figure 4. Difference photoemission spectra at N 1s edge for high-spin phase.

References

[1] P. Gutlich, *et al.*, Angew. Chem. **33**, 2024 (1994).

[2] M. Kamada *et al.*, UVSOR Activity Report **28**, 158 (2001).

(BL4B)

PES and NEXAFS study of DNA polynucleotides on silicon dioxide surfaces with and without iodine doping

Masashi Furukawa[1,2], Hiroyuki S. Kato[1], Masateru Taniguchi[2], Takaki Hatsui[3], Hiroshi Oji[3], Tadahiro Komeda[1], Tomoji Kawai[2], Nobuhiro Kosugi[3] and Maki Kawai[1]

[1] *RIKEN (The Institute of Physical and Chemical Research), Hirosawa, Wako, Saitama 351-0198, Japan*

[2] *The Institute of Scientific and Industrial Research, Osaka University, Mihogaoka, Osaka 567-0047, Japan*

[3] *Institute for Molecular Science, Myodaiji, Okazaki 444-8585, Japan*

Electrical properties of DNA double strands are being attractive as they are considered to be a candidate for the building block of functional molecular systems in nano-scale technology. Direct measurements of the electrical transport of DNA have been extensively reported, and thus it has been found out that double-stranded DNA polynucleotides with well-defined sequences, Poly(dG)·Poly(dC) and Poly(dA)·Poly(dT), show the hole-conductive and the electron-conductive behaviour, respectively ($\rho \sim 1$ Ω·cm) [1]. It has also been confirmed that the conductivity of Poly(dG)·Poly(dC) were increased by the iodine doping, i.e., hole-doping, while that of Poly(dA)·Poly(dT) were not changed [2]. In this study, both occupied and unoccupied electronic structure of such polynucleotides have been characterized by use of photoelectron spectroscopy (PES) and near-edge X-ray absorption fine structure spectroscopy (NEXAFS), aiming at the investigation of the origin of the iodine-doping effect as well as that of carrier conduction mechanism of DNA, which is currently a hot debate.

The specimens used in our experiments were synthesized DNA polynucleotides, Poly(dG)·Poly(dC) and Poly(dA)·Poly(dT), purchased from Amersham Pharmacia Biotech. DNA solutions were dropped onto SiO_2/*p*-Si(111) surfaces (ρ = 20–40 Ω·cm), blown off after the fixation for a few minutes. Iodine doping was achieved by sealing samples with elemental iodine in evacuated Pyrex glass ampoules for 6 hours. PES and NEXAFS measurements were performed at BL4B soft-X-ray beamline of the UVSOR facility, equipped with the double crystal monochrometor. NEXAFS measurements were performed by the total electron yield mode. A SCIENTA SES-200 hemispherical electron energy analyzer was utilized for the PES measurements. The PE spectra of Si 2p region (Binding energies (B. E.) of bulk of *p*-Si: 99.1 eV and SiO_2: 103.2 eV) were measured to calibrate the electron energy and intensity of the spectra.

Figure 1 shows the N 1s XP spectra of DNA polynucleotides on SiO_2/*p*-Si(111) surfaces with and without iodine doping. Two dominant components (lower B.E.: =N- and higher B.E.: -N- [3]) observed for non-doped samples were drastically changed in intensity ratio by doping iodine. For both polynucleotides with iodine doping, the intensity of higher B.E. component was stronger than that of lower one, while P 2p core levels did not show drastic differences in intensity and binding energy in their spectra (see Fig. 2). Nitrogen *K*-edge X-ray absorption spectra has also shown the significant difference between iodine-doped and non-doped polynucleotides samples, as shown in Fig. 3. As iodine were doped into DNA, second prepeak (π^*_{-N-} resonance [4]) were shifted toward the lower excitation energy, while first prepeak ($\pi^*_{=N-}$ resonance) were not shifted and

the intensity of second prepeak is stronger than the first one. It is concluded so far, from these PES and NEXAFS results, that iodine intercalates directly into the DNA base molecules (π stacking). We are currently analyzing these doping effects using molecular orbital calculations.

References

[1] K. –H. Yoo et al., Phys. Rev. Lett. **87,** 198102 (2001).

[2] M. Taniguchi et al., in preparation.

[3] L. S. Shlyakhtenko et al., Biophys. J. **77,** 568 (1999), and references therein.

[4] S. Mitra-Kirtley et al., J. Am. Chem. Soc. **115,** 252 (1993).

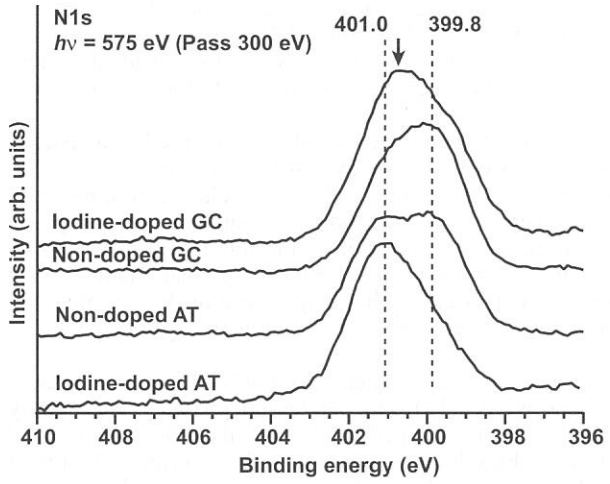

Fig. 1 N 1s XP spectra for DNA polynucleotides on SiO_2/*p*-Si(111) surfaces with and without iodine-doping ($h\nu$ = 575 eV).

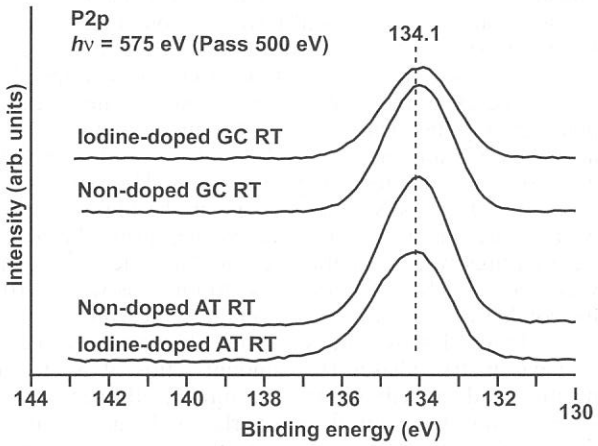

Fig. 2 P 2p XP spectra for DNA polynucleotides on SiO_2/*p*-Si(111) surfaces with and without iodine-doping ($h\nu$ = 575 eV).

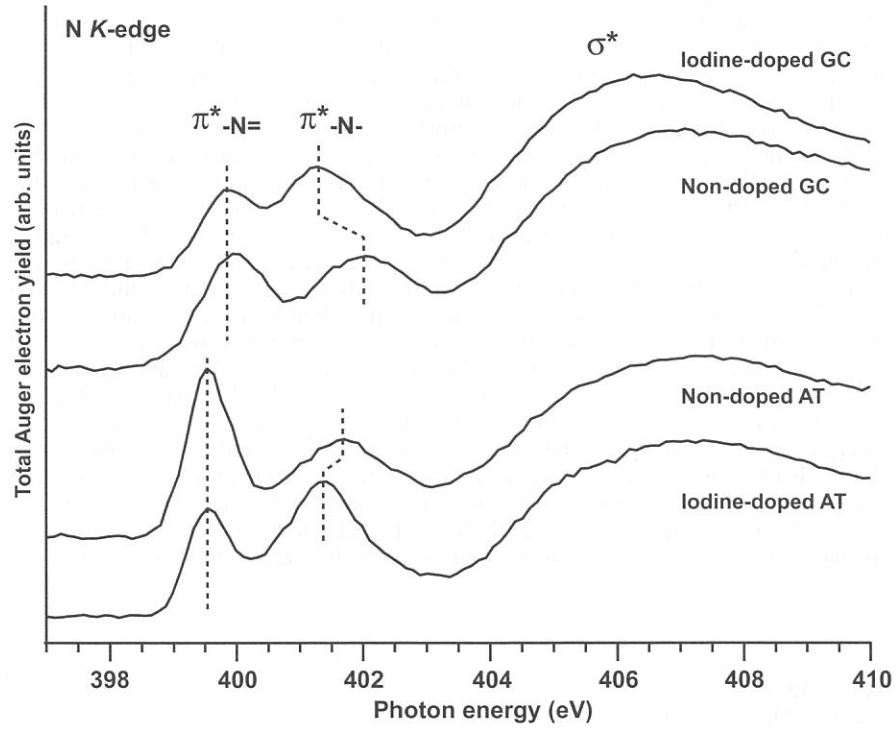

Fig. 3 Nitrogen K-edge absorption spectra spectra for DNA polynucleotides on SiO_2/*p*-Si(111) surfaces with and without iodine-doping.

(BL4B)

N 1s Photoabsorption of N_2 Trapped in Rare Gas Matrices

Mitsuru Nagasono , Hiroshi Oji, Takaki Hatsui, Eiji Shigemasa, and Nobuhiro Kosugi

Institute for Molecular Science, Myodaiji, Okazaki 444-8585, Japan

The N_2 molecule has been widely used as an ideal system to study the inner-shell excitation process. Many N 1s photoabsorption spectra have been reported for the gas phase (monomer [1-3] and clusters [4]), condensed phase [5,6], and surface-adsorbed phase of N_2 [7,8]. The gaseous N_2 spectra show a strong bound state resonance and a strong continuum resonance, even in low-resolution spectra. These features arise from the 1s-π^* excitation and the σ^* shape resonance, which are orthogonal to each other in the polarization dependence to the linearly polarized soft X-rays. The anisotropy is clearly observed in the angle-resolved photoion yield spectroscopy (ARPIS) of gaseous N_2 [1], and is used to determine the adsorption geometry of N_2 [8]. Furthermore, high-resolution inner-shell spectra of N_2 show many Rydberg excited states below the ionization threshold and several double and triple excitations near and above the threshold [2,3]. Some of them have diffuse character and should have environmental effects around the molecule. Thus, N_2 is also an ideal system from the viewpoints of the surrounding effect and of the difference between gas and solid. In the present work, we have measured N 1s excitation spectra of N_2 trapped in rare gas matrices.

The experiments were carried out at a new beamline BL4B, which is equipped with a varied-line-spacing plane grating monochromator. The monochromator was operated with an energy resolving power E/dE = 8000 at 400 eV photon energy. N 1s photoabsorption spectra were measured with an electron yield method, but with a transmission method for gaseous N_2. The rare gases used were Ne, Ar, Kr and Xe. Samples were prepared by mixing gaseous N_2 with rare gas in the high-vacuum stainless-steel vessel; before the mixing, the amounts of N_2 and rare gas were controlled by measuring the pressure in each vessel with a capacitance manometer. The gas mixtures were evaporated on an Au coated sample plate of a cryostat. The temperature of the sample plate was below 6.5 K. The ratios N_2 to rare gas were 1/10 and 1/1. Furthermore, N 1s photoabsorption spectra of the condensed and gaseous N_2 were also measured.

Figure 1 shows the N 1s photoabsorption spectra in the 1s-π^* resonance region for the N_2 in gaseous phase, rare gas matrix phases (the amount ratios of N_2 to rare gas were 1/10) and condensed phase. The energy position and the vibrational structure in all spectra are essentially unchanged, indicating that the 1s-π^* excited states do not have significant overlap with surrounding atoms. Flesch et. al. have recently reported red shift of 6 ± 1 meV of the 1s-π^* excitation in N_2 clusters relative to N_2 monomer due to dynamic stabilization that follows photoexcitaion [4]. Though there are also very small energy differences among the present data, argument about the energy shift would need more high-resolution measurement and more careful energy calibration on our spectrometer.

Figure 2 shows the N 1s photoabsorption spectra near the N 1s ionization threshold region, which contains Rydberg excitations, multiple excitations and a σ^* shape resonance. The excitations from N 1s to 3*s* and 3*p* Rydberg states are clearly identified in all spectra. The 3*s* and 3*p* excited states both exhibit blue shifts in photon energy in the matrix phase. Furthermore, compression of the Rydberg series is observed with the increasing the concentration of N_2 in the rare gas matrices. The behavior of the blue shifts is the same as that in UV photoabsorption spectra of NO trapped in the rare gas matrices reported by M. Chergui, et. al. [9].

The absolute energy for the Rydberg excitation is obtained by subtracting the term value from the ionization potential; then, the shift of the Rydberg excitation energy is determined by competition between the shifts of the ionization potential and the term value. The ionization potential becomes smaller with decreasing the distance between the N_2 and the neighbor atoms or molecules [10]. Thus the red shift of the ionization potential becomes larger as the cage size smaller. On the other hand, the term value is related to the antibonding character in the Rydberg state, and the antibonding character depends on the overlap of the Rydberg orbitals with the valence orbital of the neighbor species; that is, on the distance between the N_2 and neighbor species or the cage size. Thus the term value becomes smaller as the cage size smaller. Since the observed matrix effect exhibits a blue shift, the variation of the term value is larger than that of the ionization potential. The situation for the energy shift by the N_2 concentration effect is nearly the same as that by the cage size effect.

The double excitations near the threshold show a complicated behavior in some systems, though it is difficult to distinguish from Rydberg excitations and from other new electronic states in solid. The well-known double excitations at 415 eV can be clearly observed for all the spectra, though fine structures in the gas phase are disappeared in the matrices. However, the energy position is essentially unchanged as for the π^* resonance excitation. The σ^* shape resonance for the dense media shifts slightly to the higher energy with respect to the gas phase. The interatomic bond distance in the N_2 molecule in the matrix might be shorter than that of the gas phase.

References

[1] E. Shigemasa, et. al., Phys. Rev. A **45**, 2915 (1992).
[2] M. Neeb, et. al., Chem. Phys. Lett. **320**, 217 (2000).
[3] E. Shigemasa, et. al., to be published.
[4] R. Flesch, et. al., Phys. Rev. Lett. **86**, 3767 (2001)
[5] O. Björneholm et. al., Physica Scripta **T41**, 217 (1992)
[6] W. Wurth et. al., Physica Scripta **T41**, 213 (1992)

[7] L. Wenzel, et. al., Phys. Rev. B **40**, 6409 (1989).
[8] J. Stöhr, et. al., Phys. Rev. B **26**, 4111 (1982).
[9] M. Chergui, et. al., J. Chem. Phys. **85**, 2472 (1986)
[10] P. S. Bagus et. al., J. Electron Spectrosc. Relat. Phenom. **100**, 215 (1999)

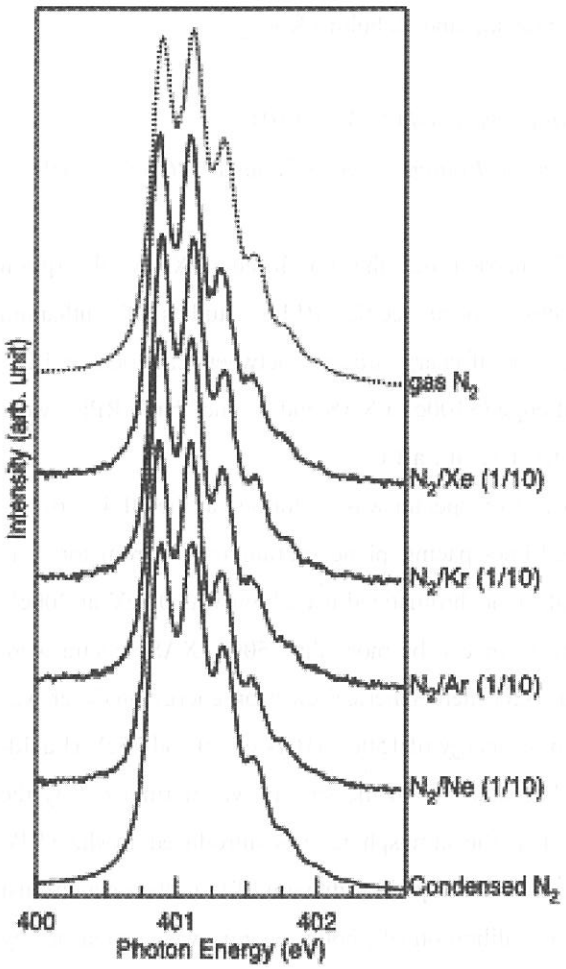

Figure 1. the N 1s photoabsorption spectra in the 1s-π^* resonance region for the N_2 in gaseous phase, rare gas matrix phases and condensed phase.

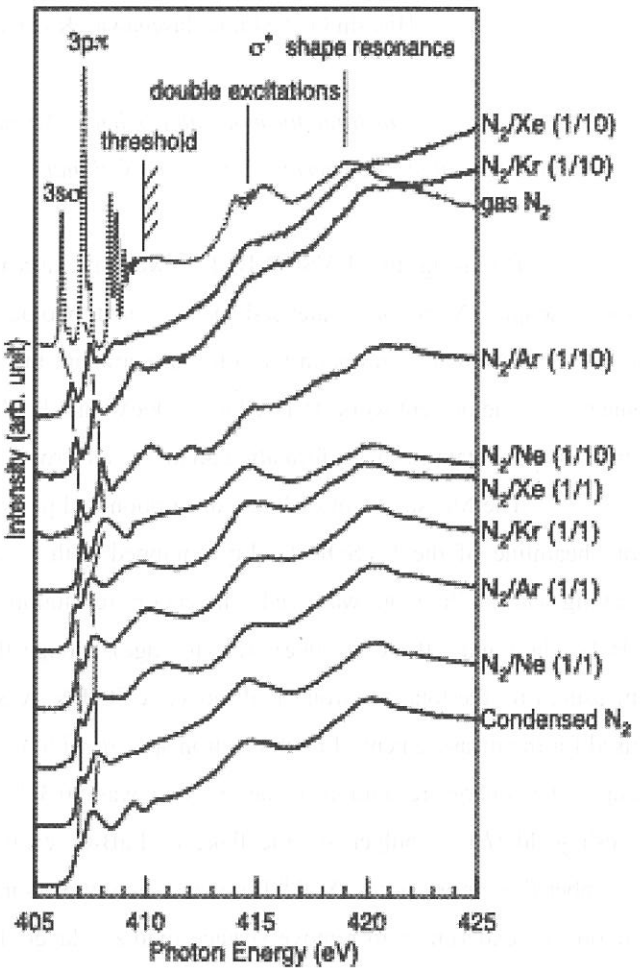

Figure 2. the N 1s photoabsorption spectra near the N 1s ionization threshold region for the N_2 in gaseous phase, rare gas matrix phases and condensed phase.

(BL4B)

B 1s- and La 4d-edge photoabsorption and Resonant Photoelectron Spectroscopy of Rare-earth Borocarbide LaB_2C_2

Hiroshi Oji,[a] Shinji Hasegawa,[a] Kazuya Suzuki,[b] and Nobuhiro Kosugi[a]

[a]*Institute for molecular Science, Myodaiji, Okazaki 444-8585, JAPAN*

[b]*Graduate School of Engineering, Yokohama National University, Hodogawa-ku, Yokohama 240-8501, JAPAN*

By using the UVSOR-BL1A, we have already carried out the La 3d-edge X-ray absorption spectroscopic (XAS) and valence-band resonant photoelectron spectroscopic (RPES) studies of lanthanum borocarbide (LaB_2C_2) to obtain the information about the dergee of charge transfer between La atoms and BC sheets.[1)] In the present work, B 1s-edge (~200eV) and La 4d-edge (~100eV) XAS and valence-band RPES were measured to obtain further information about the electronic structure of LaB_2C_2.

The Measurement of X-ray absorption and photoelectron spectra was performed at the BL4B soft X-ray beamline of the UVSOR facility equipped with varied-line-spacing plane grating monochromator. The grating with 267line/mm was used. The energy resolution of monochromatized used light was 0.1eV at 200eV (B 1s-edge) and 0.03eV at 100eV (La 4d-edge), though the $E/\Delta E$ can be more than 5000. XAS spectra were measured by the total electron yield mode. A SCIENTA SES-200 hemispherical electron energy analyzer was used for the measurement of photoelectron spectra with the pass energy of 150eV (B 1s-edge) and 75eV (La 4d-edge). The energy resolution of the analyzer was ~0.3eV. The intensity of the spectra was normalized by the mesh yield (I_0). A polycrystalline flake of LaB_2C_2 cleaved in the atmosphere was introduced in the UHV chamber (base pressure: $<3X10^{-10}$Torr), and the sample surface was scraped by diamond file in the vacuum just before the experiment to remove surface oxidized layer. The calibration of photon energy was carried out by assuming the π^* peak of h-BN as 191.8eV.[2)]

La 4d-edge XAS spectrum of of LaB_2C_2 is shown in Fig. 1. The assignments of the peaks are indicated in the figure.[3)] The valence- and inner-valence RPES spectra of LaB_2C_2 at various photon energies (indicated by numbers) are shown in Fig. 2. Abscissa corresponds to the binding energy relative to the Fermi level (E_F). La 5p bands (~20eV) are significantly enhanced in the on-resonant (La 4d) spectrum. Especially, an anomalous change of the photoemission branching ratio between $5p_{3/2}$ and $5p_{1/2}$ intensity can be seen. Actually, this anomaly is also observed in other La compounds. Ogasawara *et al.* attributed this to the multiplet dependence of the Auger transition probabilities.[3)] The intensity of the all valence- and inner-valence band begin to decrease from the photon energy of "5", and almost no structure can be observed at "10". Such a phenomenon was not observed in the RPES spectra at B K-edge as seen in Figs. 3 and 4.

References

1) See the page for BL1A.

2) R. Franke et al., *Chem. Phys.* **216** (1997) 243.

3) H. Ogasawara *et al., Solid State Commun.* **81** (1992) 645.

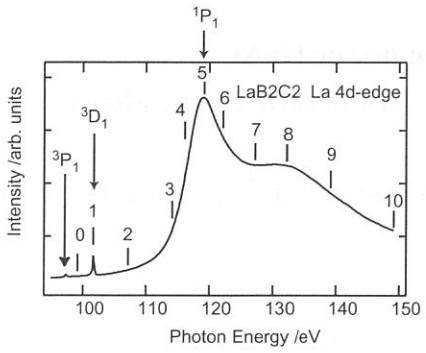

Fig. 1. La 3d-edge XAS spectrum of LaB_2C_2.

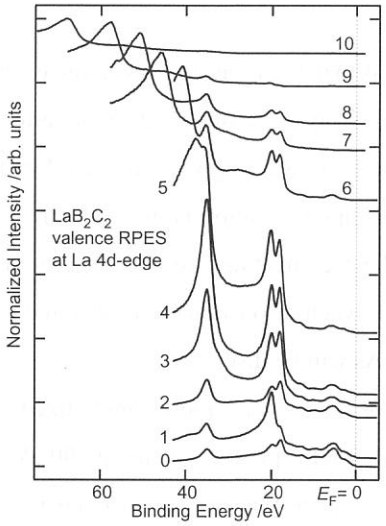

Fig. 2. The valence- and inner-valence RPES spectra of LaB_2C_2 at various photon energies.

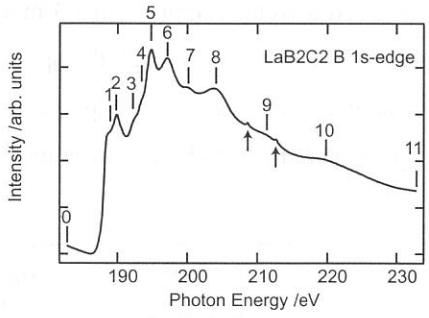

Fig. 3. B 1s-edge XAS spectrum of LaB_2C_2. (The small peaks indicated by the arrows are due to the La 3d absorption by 4th order light.)

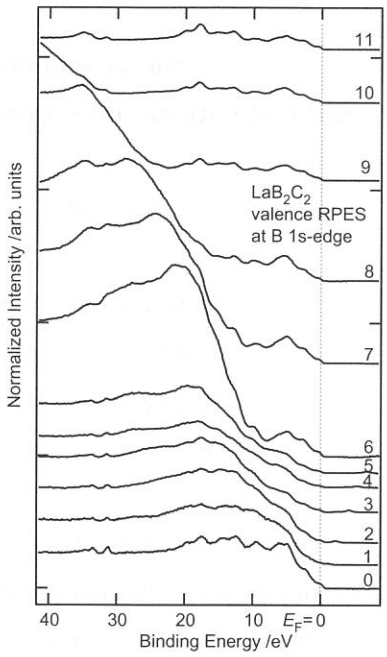

Fig. 4. The valence- and inner-valence RPES spectra of LaB_2C_2 at various photon energies.

(BL5A)

Surface photovoltage effects on n-type GaAs studied with combination of SR and laser : Temperature dependence

Senku TANAKA, Kazutoshi TAKAHASHI [A], Junpei AZUMA [B] and Masao KAMADA [C]

The Graduate University for Advanced Studies, Okazaki 444-8585

[A] *UVSOR Facility, Institute for Molecular Science, Okazaki 444-8585*

[B] *Department of Physics, Kyoto University, Kyoto 606-8502*

[C] *Synchrotron Light Application Center, Saga University, 840-8502*

The absorption of photon with energy larger than the bulk band-gap energy generates electron-hole pairs. The spatial separation of electrons and holes in the space-charge layers causes electromotive force called surface photovoltage (SPV) [1]. Recently, we proposed an approximate formula to give a simple relation of SPV with photocarrier density, temperature and initial band-bending. This approximation is in good agreement with the experimental results of the SPV effect on p-type GaAs [2]. In the present study we have measured the SPV effect on n-type GaAs using photoelectron spectroscopy combined synchrotron radiation (SR) and laser. The applicability of the approximation to the measurements of n-type GaAs will be discussed.

The experiments were performed at BL5A, UVSOR. SR was monochromatized with an SGM-TRAIN-type monochromator. The photon density was typically 3 x 10^9 photons/s·mm^2 at 100 eV. The base pressure of the experimental chamber was about 2 x 10^{-8} Pa. A hemispherical electron-energy analyzer (OMICRON EA125HR) was used for the photoelectron spectroscopy. The overall energy resolution was about 0.2 eV. We used a Ti: Sapphire laser system (COHERENT Mira 900-F) to cause the SPV effect. The wavelength of the laser was 800 nm and the repetition frequency was about 90 MHz (synchronized with SR). Laser light was transported to the experimental chamber using an optical fiber and focused onto the sample with a 3-mm radius spot. The temporal width of the laser pulses was expanded to about 100 ps by passing through the optical fiber. The spatial overlap between the laser and SR was adjusted by our eyes. We performed experiments on a Si-doped (1 x 10^{18} cm^{-3}) GaAs. The clean surface of the sample was prepared *in situ* by an annealing and ion sputtering.

Fig. 1 shows photoelectron spectra of an n-type GaAs. Solid and dotted lines represent the photoelectron spectrum with and without laser illumination, respectively. As can be seen from Fig. 1, the illumination of the laser results in a shift of the photoelectron spectrum toward lower kinetic energies. This shift originates from the SPV effect caused by the laser-excited carriers [2]. Fig. 2 shows the temperature dependence of the peak energy of the Ga-3d

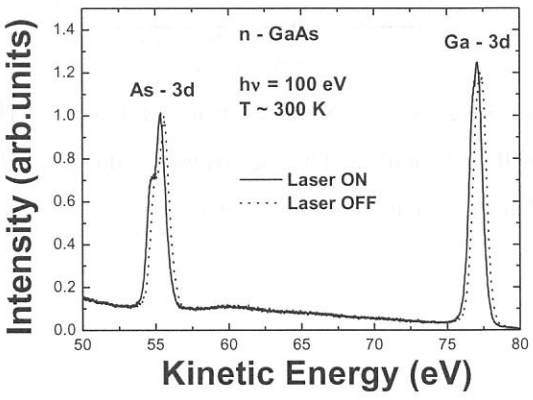

Figure 1. Effects of the laser illumination on an n-type GaAs surface.

photoelectron spectrum. Circle and triangle represent the peak energy of the Ga-3d with and without laser illumination, respectively. In the range over 350 K, the peak energy without laser illumination remains almost constant. In the range under room temperature, the peak energy shifted toward lower kinetic energies with decreasing temperature. The absolute values of the SPV shift of Ga-3d in the range of 80- 400 K are shown in Fig. 3 as dots. The SPV shift increased with decreasing temperature from 400 K to room temperature, while, the SPV shifts decreased on further cooling below ~275 K.

The present results are different from the behavior of p-type GaAs [2]. In the case of p-type GaAs, the SPV shifts increase with decreasing temperature. It is found that the peak energy without laser illumination remains nearly unaffected by the change of temperature in the p-type, while that is strongly affected in the n-type. Therefore, the temperature dependence of the initial band-bending values may explain the discrepancy of SPV shift. The simple formula of the SPV effect can be expressed as

$$\beta\Delta\Psi \exp(\beta\Delta\Psi) = \frac{\delta n}{n_0}\exp(\beta\Psi_0), \quad (1)$$

where $\beta = e / kT$, e is the absolute value of electron charge and k and T have their usual meanings, $\Delta\Psi$ is SPV, δn is photoexcited carriers, and n_0 is the doping density. From Fig.2, we can obtain the temperature dependence of the initial band-bending values. The solid line of Fig. 3 represents the simulation of SPV that includes temperature dependence of the initial band-bending values. This simulation agrees qualitatively with the experimental result. The simulation is not complete in temperature range lower than 200 K. This disagreement may be attributed to the fact that the present experimental conditions are beyond the approximation. Further consideration is in progress.

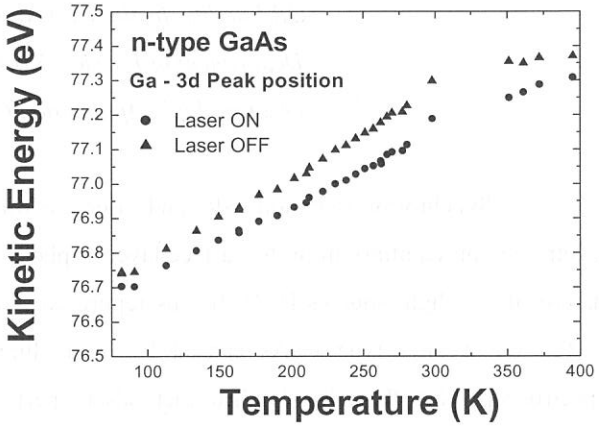

Figure 2. Temperature dependence of the peak energy of the Ga-3d photoelectron spectrum.

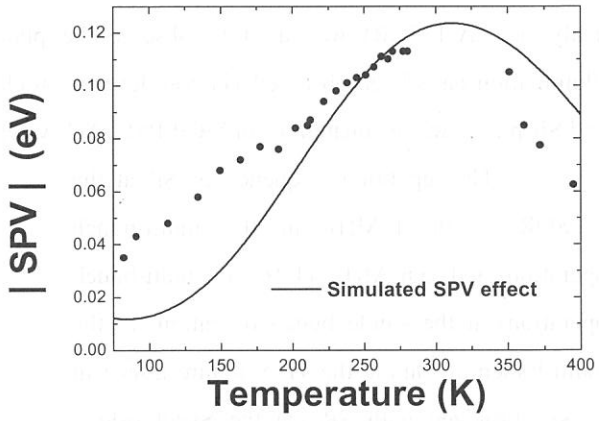

Figure 3. Temperature dependence of the SPV shifts.

In summary, we have studied the SPV effect on n-type GaAs. The simple approximate formula fairly explains the temperature dependences of the SPV in both of p-type and n-type GaAs.

References

[1] W. Mönch, *Semiconductor Surfaces and Interfaces* (Springer, 2001) 3rd ed.

[2] S. Tanaka et al., Phys. Rev. B **64** (2001) 155308.

(BL5A)

Surface photovoltage effects on n-type GaAs studied with a time-resolved photoelectron spectroscopy

Senku TANAKA, Kazutoshi TAKAHASHI [A], Junpei AZUMA [B] and Masao KAMADA [C]

The Graduate University for Advanced Studies, Okazaki 444-8585

[A] *UVSOR Facility, Institute for Molecular Science, Okazaki 444-8585*

[B] *Department of Physics, Kyoto University, Kyoto 606-8502*

[C] *Synchrotron Light Application Center, Saga University, 840-8502*

Synchrotron radiation (SR) and laser are widely used as useful light sources. We have studied the electronic non-equilibrium in the surface layer of photo-excited p-type GaAs using the combination of the pulse nature of two light sources [1-3]. In this report, we present the temporal change of the surface photovoltage (SPV) effect on n-type GaAs caused by laser illumination by means of a time-resolved photoelectron spectroscopy (TR-PES). Two kinds of methods are performed for measuring the TR-PES. One is the pump-probe method through the synchronization of SR and laser. The other uses the pick-out method through the gate circuit.

Experiments were performed at BL5A. A Si doped (1 x 10^{18} cm^{-3}) n-type GaAs was used for the measurements. We used the Ti: Sapphire laser (COHERENT Mira 900-F) and the regenerative amplifier (COHERENT RegA) as the excited light sources to cause the SPV effects. The OMICRON electron-energy analyzer (EA-125HR) was used to observe the photoelectron spectra. The SPV effects caused by laser illumination have been observed via core-level photoelectron spectra [3, 4]. The temporal overlap of the laser and SR pulses was evaluated by an MCP-PM/TAC system.

The repetition frequency of SR at the UVSOR is 90.115MHz in the multi-bunch operation and 5.63MHz (1/16 of multi-bunch operation) at the single bunch operation. In the multi-bunch operation, the Ti: Sapphire laser can be synchronized with SR via the Synchro-lock circuit. We obtain the TR-PES in the range of 11ns using this system. In the single bunch operation, if the laser pulses could be picked out via the AO modulator to synchronize with SR, the range of about 176 ns would be allowed to observe the TR-PES. Time resolution of the pump-probe method is restricted by the SR pulse width and it is typically about 1.5 ns.

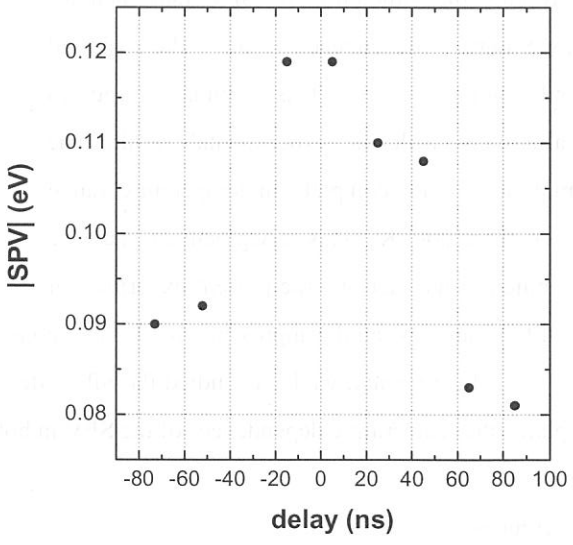

Figure 1. Time dependence of the SPV on an n-type GaAs.

Fig. 1 shows the measurement of the time dependence of SPV on n-type GaAs in the single bunch operation with different delays between the laser

and SR pulses. One can see the increase of the SPV around zero delay and it decreases gradually with time. We can also distinguish that the SPV lifetime is longer than 176 ns. Here we would like to emphasize that the laser pulses was not completely picked out to one by one ratio for a single SR-pulse because the rise time of the AO modulator were lager than 11ns. Although, a single pulse was not completely picked out, the pulse train of laser light was synchronized with an SR pulse.

The regenerative amplifier gave the laser light with the frequency of 10 to 300 kHz. The combination of this laser light and the gate system can provide TR-PES in the microsecond range. The gate circuit receives the photoelectron signal from the electron energy analyzer and the trigger signal from the laser system. The gate system can pick out the time-window for the time width in the range from 40 ns to 160 μs. The time resolution of this system is restricted by the time width of the photoelectron signals, which is about 0.1 μs. In Fig. 2 we present the TR-PES Ga-3d photoelectrons. The Ga-3d photoelectron spectrum without laser illumination is also shown for comparison. The frequency of the laser was 100 kHz. It can be seen that the Ga-3d photoelectron spectrum is shifted toward lower kinetic energies due to the SPV effects caused by laser illumination. It is also obvious that the shift value decreases with the delay time. The analyses in detail, such as the curve fitting of the core-level spectra and time constant of the SPV decay time, are now in progress.

To summarize, we have performed the time dependent experiments of the SPV effects on an n-type GaAs using the TR-PES. It was observed that the temporal change of the SPV effects in the range from nano-second to microsecond. These experimental results provide the better understanding for the dynamics of the SPV effects.

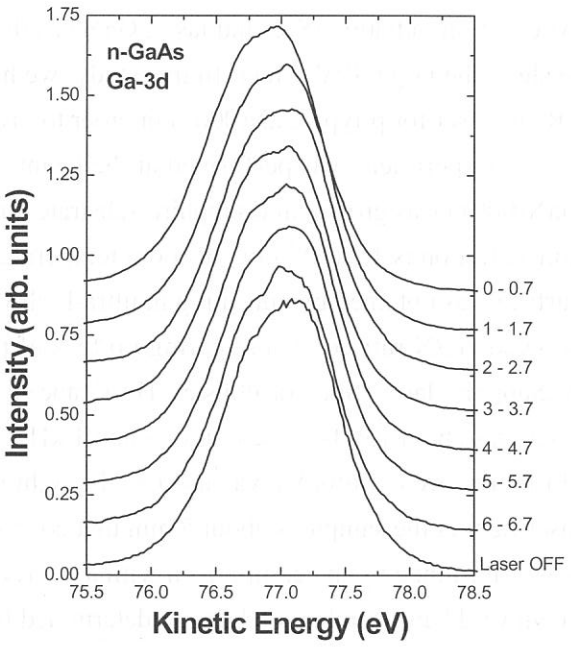

Figure 2. The time-resolved photoelectron spectra of the Ga-3d core-levels. Each figures of right side represents the pick out time in microsecond unit. The spectrum without laser illumination is shown for comparison.

References

[1] M. Kamada et al., UVSOR Activity Report, 1999, 180.

[2] S. Tanaka et al., UVSOR Activity Report, 2000, 154.

[3] S. Tanaka et al., Phys. Rev. B **64** (2001) 155308.

[4] S. Tanaka et al., UVSOR Activity Report, 2000, 152.

(BL6A2)

Surface photo-voltage effect on GaN(0001) studied by photoemission spectroscopy with the combination of SR and Laser

Kazutoshi Takahashi[A], Kousuke Hayakawa[B], Senku Tanaka[C], Junpei Azuma[D], Minoru Itoh[B], and Masao Kamada[E]

[A] *UVSOR Facility, Institute for Molecular Science, Okazaki 444-8585*
[B] *Department of Electrical & Electronic Engineering, Shinshu University, Nagano 380-8553*
[C] *The Graduate University for Advanced Studies, Okazaki 444-8585*
[D] *Department of Physics, Kyoto University, Kyoto 606-8502*
[E] *Synchrotron Light Application Center, Saga University, Saga 840-8502*

Surface photo-voltage (SPV) effects on semiconductor surface have been attracting considerable interest from the viewpoints of surface physics and practical applications for photo-electronic devices. Recently, several researchers have reported the SPV effects on Si(111) [1] or GaAs(100) [2] surfaces using the core-level photoemission spectroscopy with the combinational use of synchrotron radiation (SR) and laser. GaN has the large band-gap energy of 3.4 eV, thus it is expected to show the large SPV effect. In this study, we have performed the photoemission spectroscopy with SR and laser for p-type GaN(0001) in order to investigate SPV effects on GaN.

Experiment was performed at the beamline BL6A2, UVSOR Facility. The p-type Mg doped GaN(0001) was grown on a sapphire substrate with AlN buffer layer using MOVPE method. The hole concentration is 1.3×10^{17} cm^{-3} at room temperature determined by the Hall measurements. The clean surface was obtained by annealing in ultra-high vacuum at about 1000°C. X-ray photoelectron spectra showed Ga/N ratio of 1, indicating no loss of the nitrogen atom after the annealing. We used the Ti:Sapphire laser (Spectra-Physics, Hurricane) to cause the SPV effect. The output of the Ti:Sapphire laser was about 130 fs pulse duration and 1 kHz repetition rate. The third harmonic of the output from Hurricane ($h\nu$ = 4.66 eV) was used as the light source to cause the SPV effect. The diameter of the laser light at the sample is about 5 mm that covers the beam spot of SR. The Fermi level of the sample was determined by the comparison with a Au reference. It is found that the present sample shows the downward band-bending of 1.26 eV determined from the valence-band spectrum.

Figure 1. shows Ga 3d photoemission spectra of GaN(0001). Solid and dotted lines represent the spectra with and without laser irradiation, respectively. The intensity of the laser light is about 0.5 mW/cm^3. As shown in Fig. 1, the Ga 3d core-level shifts to the higher kinetic energy side under the irradiation of laser. It is also found that the spectral shape does not change with laser irradiation. In conjunction with our previous results for GaAs, it is considered that the observed peak shift originates from the SPV effect due to the spatial separation of electrons and holes excited by absorption of laser light in the space-charge region.

Figure 2 shows the dependence of the peak shift on the laser intensity. In Fig. 2, positive direction of peak shift corresponds to the shift to higher kinetic energies and the laser intensity of 100% corresponds to 50 mW/cm^2. As shown in Fig. 2, the peak shift due to the SPV effect increases with increasing laser intensity from 0.015% to about 1%. On the other hand, it is found that peak shift decreases with increasing laser intensity at the laser intensity above 5%, and finally Ga 3d peak shows

negative peak shift at the laser intensity of 50 and100 %. We found that the observed dependence on the laser intensity in the low laser intensity region less than 1% fits well with the theoretical relation between laser intensity and SPV effect which is described in detail elsewhere [3]. In this theoretical model, we assumed that the amount of the photo-excited carriers is in proportion with laser intensity and distribution of the surface state is uniform. It has been reported that this approximation is in good agreement with the experimental result of the SPV effects on p-GaAs(100). However, the dependence in the higher laser intensity region cannot be explained by the present simple formula. In order to fully explain the laser intensity dependence, the change of the surface electronic charge caused by many amounts of photo-excited carriers should be considered. Further investigations including the time-resolved measurement are needed to elucidate the SPV effects on GaN surface in detail.

In conclusion, we have performed the photoemission study for the SPV effects on p-GaN(0001) using synchrotron radiation and laser. It is found that Ga 3d core-level spectra show the peak shift due to the SPV effect. The dependence of the peak shift on the laser intensity at the laser intensity less than 0.5 mW/cm^2 can be explained by simple formula.

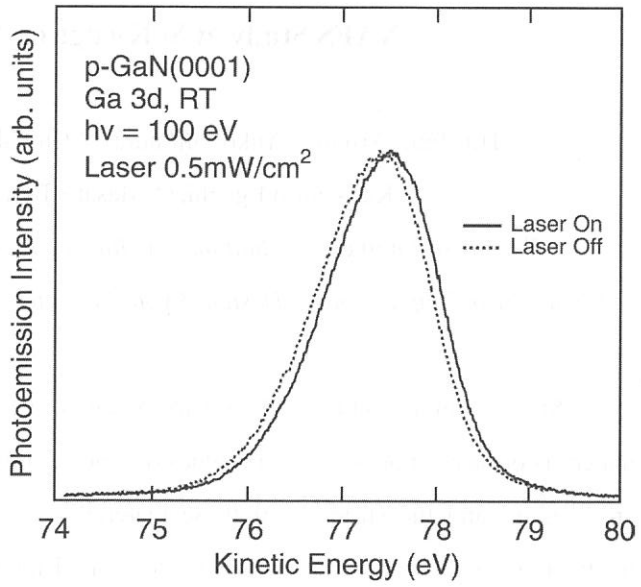

Figure 1. Ga 3d photoemission spectra with and without laser irradiation for p-GaN(0001).

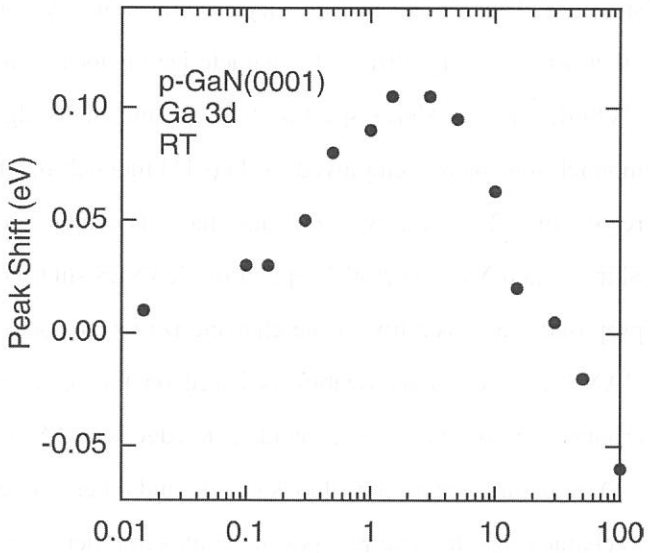

Figure 2. Laser intensity dependence of the peak shift due to the SPV effect on p-GaN(0001).

References

[1] J. P. Long *et al.* Phys. Rev. Lett. **64**, 1158 (1990).

[2] M. Kamada *et al.* Sur. Sci. **454-456**, 525 (2000).

[3] S. Tanaka *et al.* Phys. Rev. B **64**, 155308 (2001).

(BL7A)

XAFS Study at Si K-edge on Several Types of Zeolites

Hirofumi Aritani,* Yuko Fujimura,** Chikako Karatani,** Takayuki Murakami,**
Ken-ichiro Eguchi,** Masato Tamai,** and Atsushi Nakahira**

**Faculty of Engineering, Saitama Institute of Technology, Okabe, Saitama 369-0293, Japan.*;

***Faculty of Engineering & Design, Kyoto Institute of Technology, Sakyo-ku, Kyoto 606-8585, Japan.*

Silica-alumina (SiO_2-Al_2O_3) binary oxide is one of the typical compounds for use of fundamental materials or basic supports. Several types of silica-alumina materials such as aluminosicicates and mullites are present, and the structure of these materials is almost depend on the Si/Al ratio and heat-treated temperature. Zeolite materials with very low Si/Al ratios are well known as microporous ones, and have been applied widely to several engineering processes because of peculiar surface activity. Zeolites are open framework aluminosilicates consisting of SiO_4 and AlO_4 tetrahedra, interconnected *via* oxygen atoms. There are several types of zeolites (MFI, MOR, BEA, *etc.*) with original types of ordered framework structure. Thus the local symmetry around Si and Al ions in these zeolites is slightly different from each other. But it is very difficult to characterize the local structure around Si and Al ions. In BL7A beamline of UVSOR, clear XANES spectra at Al K- and Si K-edges have been obtained since YB_{66} double-crystal monochromator was employed.[1] KTP(011) monochromator gave more emission of soft X-ray source in the region of 1.2 - 2.1 keV,[2] and thus, more accurate XANES spectra can be obtained. In recent studies, Shimizu and Yoshida et al.[3] applied the XANES study to evaluate the local structure around Al ions. They proposed the possibility of the characterization of local structure by means of edge energy in Al K-edge XANES. This characterization is based on the relationship between the energy and the local structure around Al ions. On the other hand, Si K-edge XANES can give an information about the local symmetry of SiO_4 structure, reported by Tanaka et al.[3] and other workers. In our study, XANES at Si K-edge was applied to characterize the several types of zeolites in order to evaluate the possibility of characterization around Si atom. Another study of Al K-edge XAFS on these materials will be reported elsewhere.[5]

For zeolite samples, H-MOR (synthesized, [I]Si/Al_2=10 and [II]Si/Al_2=18), H-MFI ([I]Tosoh JRC-Z-1000H (Si/Al_2=1000) and [II]Tosoh HSZ-890H0A (Si/Al_2=1880)), H-BEA (JRC-HBEA-25, Si/Al_2=25) were employed. Quartz, Silica-gel, and silicic acid (SiO_2•xH_2O) were used for silica reference samples. The XANES at at Al K- and Si K-edges were measured in BL7A of UVSOR in a total electron yield mode at ambient temperature by using KTP(011) monochromator.

Figure 1 (Top) shows the Si K-edge XANES spectra of reference Si compounds. SiO_4 tetrahedra with T_d symmetry are dominant in quartz. The SiO4 tetrahedra in silica-gel and silicic acid contain several types of vacancy sites and/or hydrated species partly, and thus, mean symmetry of SiO_4 local structure is

lower than that of T_d structure in quartz. The prominent peak in XANES centered at 1853 eV is due to $1s$ - $3p$ electron in Si atom. In symmetric SiO_4 (T_d) tetrahedron, monolithic state of $3p$ band energy is present. In case of lower symmetry, the band should be broader, and intensity of the prominent peak should be lower. The results of XANES spectra indicate the structural feature about the lower symmetry in silica-gel and silicic acid than that in quartz. This structural result can hardly be obtained by means of other spectroscopy.

Middle of the figure shows the XANES of MOR zeolites. These results show the independence between the Si/Al atomic ratio and local symmetry in SiO_4 tetrahedra. These tetrahedra have low symmetry than silicic acid. Thus it is clear that local structure around Si in MOR framework has low symmetry by formation of mordenite structure with three-dimensional micropore. This feature is also seen in the XANES results of H-MFI. In contrast, intensity of the peak in H-BEA (with thenty-menbered ring in local framework) is larger than that in silicic acid, indicating the higher symmetry than in MOR or MFI. From these results, local symmetry around Si atom in zeolites depends on the framework structure of zeolites. It is likely that small pore size(s) and low-membered rings in the framework tend to give low symmetry in SiO_4 tetrahedra. Detailed characterization on zeolites and silica-alumina materials are now in progress. This work is partly supported by Asahi Glass Fundation.

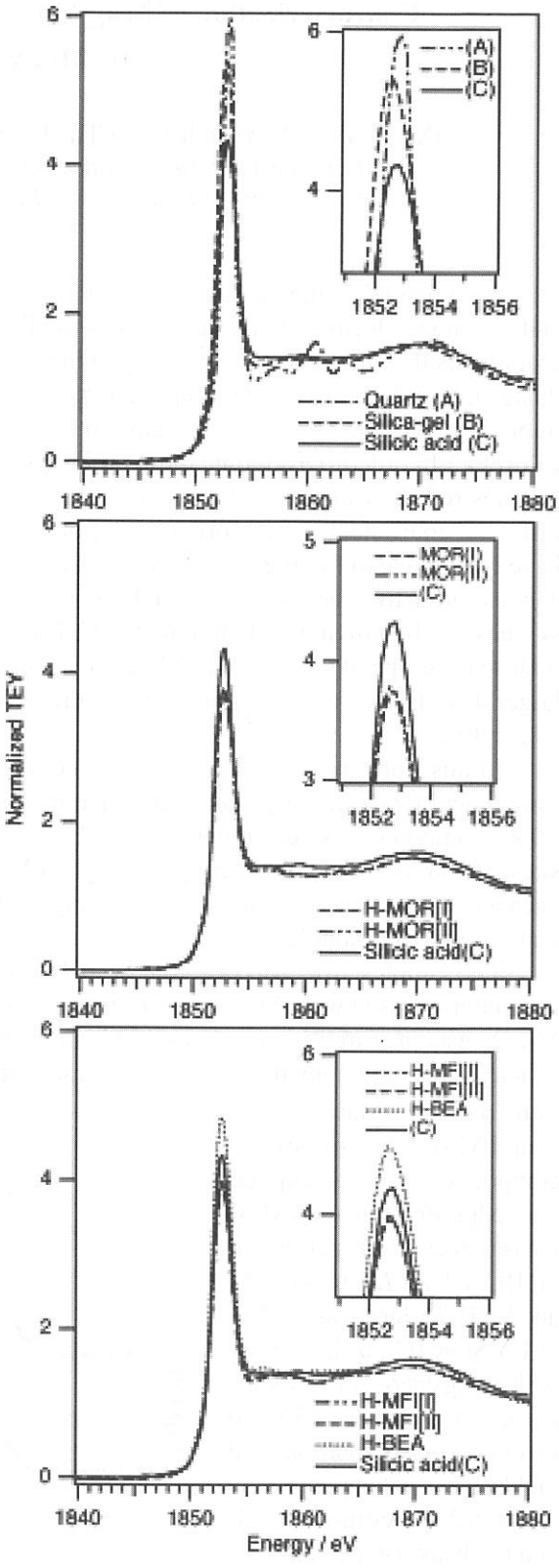

Fig. 1 Si K-edge XANES spectra of reference silica-type materials (top), H-MOR (middle), H-MFI, and H-BEA zeolites (bottom).

References

1. T. Kinoshita et al., *J. Synchrotron Rad.*, 5 (1998) 726.
2. Y. Takata et al., *J. Synchrotron Rad.*, 8 (2001) 351.
3. K. Shimizu et al., *Chem. Commun.*, **1996**, 1681.; H. Yoshida et al., *UVSOR Activity Report*, **1999**, 148.
4. T. Tanaka et al., *J. Phys. IV (Colloq. C2)*, **1997**, 913.
5. H. Aritani et al., *Chem. Mater.*, in press.

(BL7A, BL8B1)

Characterization of $Mn_{1-x}Mo_{2x}V_{2(1-x)}O_6$ as anode for Li Secondary Battery by Mo, V and Mn L-XANES

Daishu HARA, Yoshiharu UCHIMOTO, Hiromasa IKUTA, and Masataka WAKIHARA
Department of Applied Chemistry, Graduate School of Science and Engineering, Tokyo Institute of Technology, 2-12-1 Ookayama, Meguro-ku, Tokyo 152-8552, Japan

Commercial available lithium ion batteries consist of two Li-intercalation materials in both for cathode and for anode electrode materials. One is the lithiated transition metal oxide as the cathode, and the other is graphite as the anode. However, the graphite anode suffers from small capacity per unit weight (about 350 $Ahkg^{-1}$). Furthermore to attain rapid charge-discharging, the rate capability of graphite material needs to be improved, because of its poor lithium ion diffusion coefficient which is much lower than that of $LiCoO_2$ or $LiMn_2O_4$. In order to overcome these problems about the capacity and rate performance of graphite material, it is desired to synthesize novel anode materials having large capacity and high rate with high lithium ion diffusion coefficient. Therefore, considerable amount of attempts such as oxide, nitrides and intermetallics have been made to finding out alternative anode materials in place of graphite anode. Among them, the oxide anode is attractive because of their high capacity. In previous paper, we proposed novel oxide anode of MnV_2O_6 synthesized by polymer gellation method. The MnV_2O_6 compound had monoclinic brannerite type structure with space grope of *C2/m*, and exhibited reversible capacity of about 800 $Ahkg^{-1}$ which is more than two times larger than that of graphite. Furthermore, the brannerite MnV_2O_6 compound had better rate property than that of graphite.

In this study, we synthesized Mo doped MnV_2O_6 ($Mn_{1-x}Mo_{2x}V_{2(1-x)}O_6$ (x=0, 0.4)) by conventional solid-state reaction and investigated electrochemical properties. The crystal structure of $Mn_{1-x}Mo_{2x}V_{2(1-x)}O_6$ ($0 < x < 0.45$)compound has been reported that Mn and Mn vacancies are randomly distributed over the original Mn sites, V and Mo randomly occupy the original V sites in the parent MnV_2O_6. Therefore, we expect that these vacancies on Mn sites might work effectively for Li ion diffusion, which leads to higher rate performance than that of un-doped sample.

The samples, $Mn_{1-x}Mo_{2x}V_{2(1-x)}O_6$ (x=0, 0.4) were prepared by conventional solid-state reaction. The starting materials used were Mn_2O_3, V_2O_5 (99.9 % Soekawa chemicals) and MoO_3 (99.9 % Soekawa chemicals). Mn_2O_3 was prepared by pyrolysis of $MnCO_3$ (99.9 % Soekawa chemicals) at 600°C for 1day in air atmosphere. The stoichiometric amounts of these materials were mixed and ground in an agate mortar. To determine oxidation states of Mn, V and Mo on the synthesized compounds, X-ray absorption near edge structure (XANES) measurements were performed on BL8B1 for *L*-edges of Mn and V, BL7A for *L*-edge of Mo at UVSOR (Okazaki, Japan) with a ring energy of 750 MeV and a stored current of 70-220 mA in a mode of total electron yields at room temperature.

CR2032 coin-type cell and the beaker-type cell were selected for charge-discharge measurement. The working electrode was fabricated by doctor-blade technique on a copper-foil, spreading paste

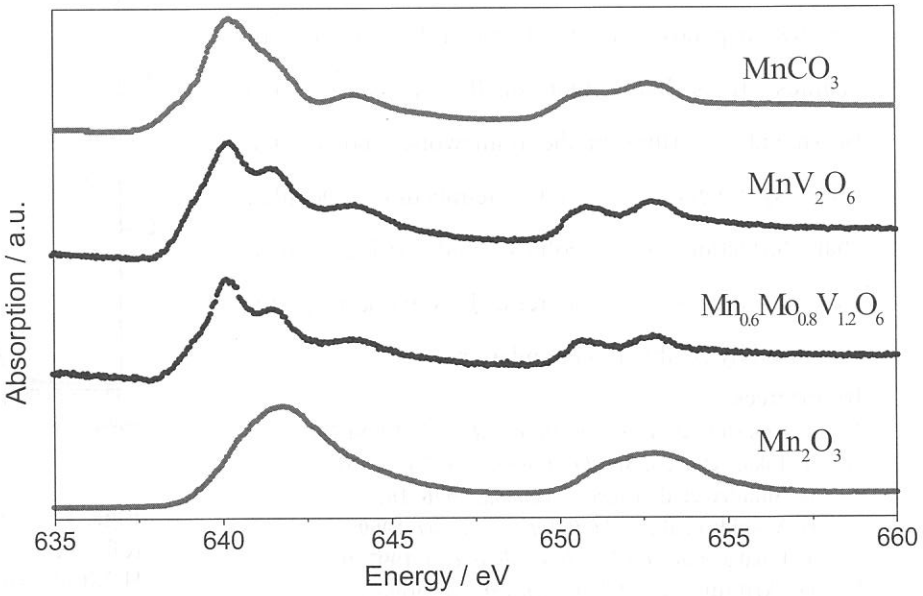

Fig.1. Mn *L*-edge XANES spectra for $Mn_{1-x}Mo_{2x}V_{2(1-x)}O_6$ (x=0, 0.4), $MnCO_3$ and Mn_2O_3.

consisted of 10 wt% polyvinylidenefluoride (PVDF) binder, 20 wt% acetylene black (conductive agent), 70 wt% active material of $Mn_{1-x}Mo_{2x}V_{2(1-x)}O_6$ (x=0, 0.4) and appropriate amount of n-metyl-2-pyrrolidinone (NMP) as solvent. After evaporating of NMP solvent in a furnace at 110°C in air atmosphere for 1day, the electrodes were roll-pressed and cut into disks. Lithium metal was used as the counter electrode. The electrolyte was 1M $LiClO_4$ dissolved in ethylene carbonate (EC) / diethyl carbonate (DEC) (volume ratio of 1:1) (received from Tomiyama pure chemical industries LTD.). All the cell assembling (Li | 1 M $LiClO_4$ in EC / DEC | $Mn_{1-x}Mo_{2x}V_{2(1-x)}O_6$ (x=0, 0.4)) was operated in a glove box filled with argon gas. The electrochemical measurements were carried out galvanostatically at various current densities at room temperature. Relaxation time between charge and discharge was set at 20 minutes.

L-edge XANES measurements of Mn, V and Mo for synthesized powdered $Mn_{1-x}Mo_{2x}V_{2(1-x)}O_6$ (x=0, 0.4) were carried out in order to investigate the oxidation states of Mn, V and Mo in the compounds. Fig. 1 shows the Mn L_{III}-edge XANES spectra of $Mn_{1-x}Mo_{2x}V_{2(1-x)}O_6$ (x=0, 0.4) together with those of $MnCO_3$ (Mn^{2+}) and Mn_2O_3 (Mn^{3+}) as references. The spectra in the figure show strong absorption features due to the spin-obit splitting of the Mn 2*p* core hole around 640 eV, and they correspond to the transition from $Mn2p^63d^n$ to $Mn2p^53d^{n+1}$. Mn L_{III} absorption peaks of $MnCO_3$ and Mn_2O_3 are apparent about 640 eV and 642 eV, respectively. This result indicates that the Mn L_{III} absorption edge shifts to higher energy with increasing the oxidation state of manganese. Both synthesized MnV_2O_6 and $Mn_{0.6}Mo_{0.8}V_{1.2}O_6$ exhibit the same feature of the spectra. Since the spectra of the edge jumps for $MnCO_3$ and $Mn_{1-x}Mo_{2x}V_{2(1-x)}O_6$ (x=0, 0.4) are very close to each other, Mn ions exist as close to Mn^{2+} in $Mn_{1-x}Mo_{2x}V_{2(1-x)}O_6$ (x=0, 0.4) compound. However, small peaks which correspond to Mn^{3+} are observed around 642 eV. Accordingly, small amount of Mn^{3+} beside main Mn^{2+} may include in the solid solution $Mn_{1-x}Mo_{2x}V_{2(1-x)}O_6$ (x=0, 0.4).

V L_{III}-edge XANES spectra of V_2O_5(V^{5+}), $VOSO_4$(V^{4+}) and $Mn_{1-x}Mo_{2x}V_{2(1-x)}O_6$ (x=0, 0.4) presented in Fig. 2 illustrate that the valence of V in $Mn_{1-x}Mo_{2x}V_{2(1-x)}O_6$ (x=0, 0.4) should be +5, because of very similar behavior of $Mn_{1-x}Mo_{2x}V_{2(1-x)}O_6$ (x=0, 0.4) and V_2O_5.

In the same way, Mo L_{III}-edge spectra of MoO_3 (Mo^{6+}) and $Mn_{0.6}Mo_{0.8}V_{1.2}O_6$ in Fig. 3 designate that the Mo oxidation state is +6 in $Mn_{0.6}Mo_{0.8}V_{1.2}O_6$ compound. In the absorption of Mo L_{III}-edge of MoO_3 and $Mn_{0.6}Mo_{0.8}V_{1.2}O_6$, the spectra split into two peaks due to splitting of d-orbital. In a pseudo-octahedral coordination, the first peak (t_{2g}) dominates, while in a pseudo-tetrahedral coordinates, the second peak (t_2) dominates. Consequently, Mo is coordinated pseudo-octahedrally with oxide ions in brannerite structure of $Mn_{0.6}Mo_{0.8}V_{1.2}O_6$.

In order to investigate the electrochemical performance of $Mn_{1-x}Mo_{2x}V_{2(1-x)}O_6$, (x=0, 0.4), the cells was subjected to charge-discharge cycles in constant current mode of 0.2 C. Cutoff voltage was set at 0.01 V and 2.50 V. The insertion process of Li into the active materials is defined as charge process, while the reverse holds for extraction process. The first Li insertion in MnV_2O_6 shows a large capacity of about 1000 $Ahkg^{-1}$ and that of $Mn_{0.6}Mo_{0.8}V_{1.2}O_6$ is about 1400 $Ahkg^{-1}$, these capacities are much larger than that of graphite (about 350 $Ahkg^{-1}$). Furthermore, $Mn_{0.6}Mo_{0.8}V_{1.2}O_6$ has larger charge-discharge capacity than that of MnV_2O_6.

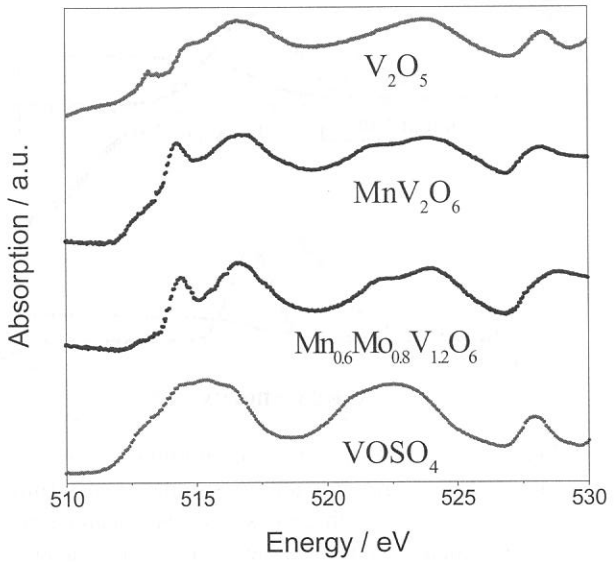

Fig.2. V *L*-edge XANES spectra for $Mn_{1-x}Mo_{2x}V_{2(1-x)}O_6$ (x=0, 0.4), V_2O_5 and $VOSO_4$.

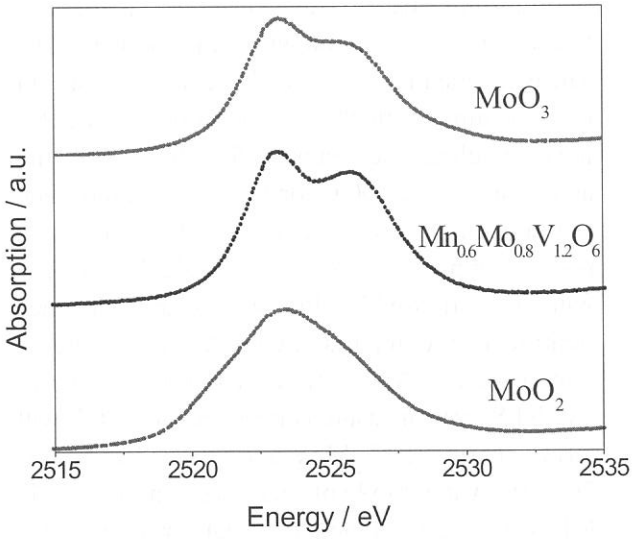

Fig.3. Mo *L*-edge XANES spectra for $Mn_{0.6}Mo_{0.8}V_{1.2}O_6$, MoO_2 and MoO_3.

(BL7A)

Al K-edge XANES of Surface Treated Natural Graphite by Aluminum

Sung-Soo KIM, Yoshihiro KADOMA, Hiromasa IKUTA, Yoshiharu UCHIMOTO and Masataka WAKIHARA

Department of Applied Chemistry, Graduate School of Science and Engineering, Tokyo Institute of Technology, 2-12-1 Ookayama, Meguro-ku, Tokyo 152-8552, Japan

Natural graphite can be thought as promising candidates for anode in lithium ion battery in terms of cost. However, it has been difficult to control the key parameters of carbon that affect their characteristics for use as anode because carbon materials have large variations in their electrical properties. Furthermore, it has been known that natural graphite flakes cannot deliver reasonable electrochemical performances such as reversible specific capacity, cycle life, rate capability, etc. Since an electrochemical reaction takes place on the surface of electrode, the control of surface properties can be thought as one of the critical factors. Therefore it needs to consider improvement by control surface properties that affect the electrochemical property of natural graphite. In this report, we investigated the influence of surface and/or structure modification by aluminum compound on electrochemical performances of natural graphite as anode in lithium ion battery. Furthermore the correlation between the local structure of amorphous-like aluminum oxide and electrochemical performance will be discussed with the results of Al *K*-edge XANES measurement.

The Aluminum-treated samples were prepared by aluminum tri-etoxide($Al(OC_2H_5)_3$, Soekawa Chemicals) treatment on NG2(Kansai chemicals). The NG2 graphite was soaked in ethyl alcohol solution containing 10wt% aluminum tri-etoxide, followed by ultrasonic treatment for 3 hours, filtration and drying above 200°C for 1 day in air atmosphere to remove residual of alcohol. On the other hand, pristine sample also prepared by alcohol soaking without Al tri-etoxide, ultrasonic treatment and heat treatment for comparison with Al-treated one. Al *K*-edge X-ray Absorption Near Edge Structure (XANES) were measured on BL7A at UVSOR with a ring energy of 750MeV and a stored current of 70-220mA in a mode of total electron yields. The KTP double crystal monochromator was used. The monochromator scanning angle step width was 0.003°, which corresponds to *ca.* 0.1eV at 1560eV.

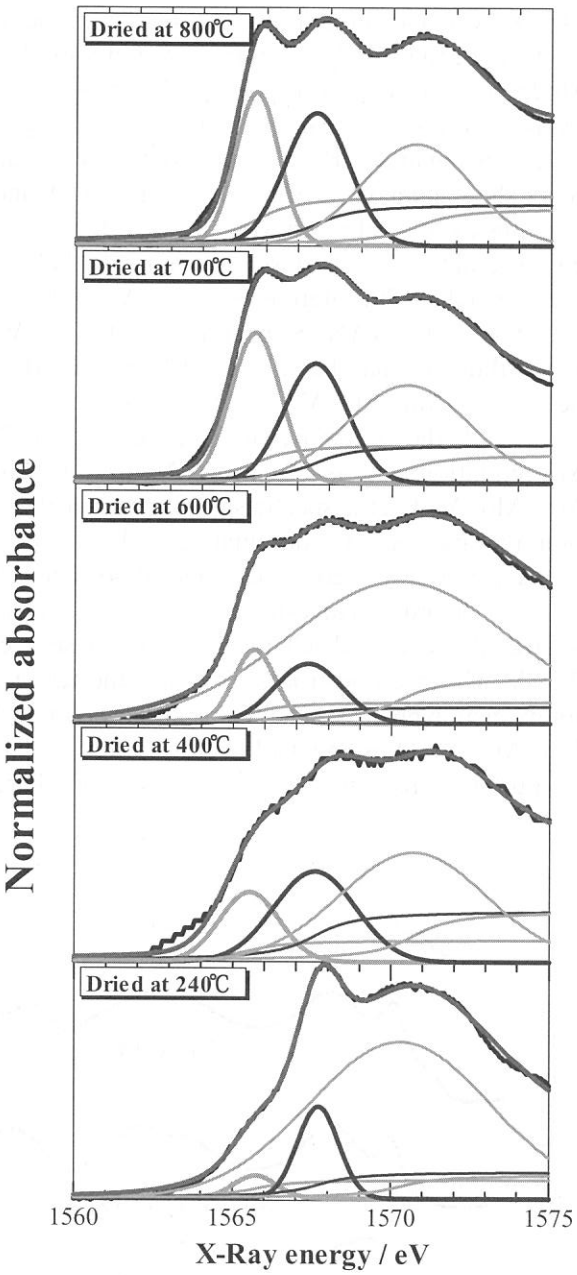

Fig.1. Al *K*-edge spectrum of alumina on the surface of natural graphite and its simulated spectrum which composed of three sets of Gaussian and arctangent function. Each samples were calcined at 800 ℃, 700℃, 600℃, 400℃ and 240℃.

The absolute energy scale was calibrated by using literature value of Al *K*-edge in α-Al_2O_3. The curve fitting for obtained XANES spectra was carried out with the REX2000 software by Rigaku.

The electrochemical measurement was carried out with the use of CR2032 coin-type cell. The working electrodes were prepared by doctor-blade technique on copper foil, spreading paste consisted of 10wt% polyvinylidenefluoride(PVdF) as binder, 10wt% acethylene black as conductive agent, 80wt% treated or pristine NG2 graphite and appropriate amount of 1-methyl-2-pyrrolidinone(NMP) as solvent. After drying of NMP solvent, the electrode was cut into disk (the weight of all sample was controlled around 4mg). Lithium metal was used as counter electrode. The electrolyte used was 1M $LiClO_4$ dissolved in ethylene carbonate(EC)/diethylene carbonate(DEC)(volume ratio 1:1). The cell assembly was operated in a glove box filled with argon gas. The specific capacity was measured by galvanostatically with current density 70mA/g, 175mA/g and 350mA/g in the ranges 0 to 2.5V on Hokuto Denko charge-discharge tester.

To investigate the correlation of Electrochemical performances with the local structure of alumina, we measured the Al *K*-edge XANES and electrochemical performance, especially in high rate Li intercalation/deintercalation to clear comparison, of samples which surface treated in different heat treatment temperature, because the structure of amorphous aluminum oxide is sensitive the preparation temperature. Since the accurate structures of alumina are not known except q-Al_2O_3, the structural analysis of amorphous-like alumina is not so simple. Recently, Al *K*-edge XANES measurement combining quantitative analysis was proposed to estimate the local structure of alumina[1]. It is well known that the XANES spectra of AlO_4 tetrahedra and AlO_6 octahedra were clearly identified in aluminum oxide. A white line 1566eV is characteristics of AlO_4 compound and the peaks at 1568eV and 1572eV can be assigned to AlO_6 octahedral compound. Normalized XANES spectra with the calcination temperature of the Al-treated graphite samples together with reference sample of α-Al_2O_3 (corundum) are shown in Fig. 1. The peak ratio of tetrahedral AlO_4 to octahedral AlO_6 in the XANES spectrum of $f¿$-Al_2O_3 (corundum) in our measurement is 7:93, which is in good agreement with that of Reference 1. We can observe a peak at 1565eV due to AlO_4 and two peaks at 1567eV and 1570eV due to AlO_6 and the difference of peak position between AlO_4 and AlO_6 was about 2eV. In addition, the relative intensity of AlO_4 and AlO_6 was varied with the calcination temperature. In the range of this study up to the 500°C of calcination temperature, the portion of AlO_4 increased, like that of previous report , this alumina phase can be thought as boehmite + g type alumina. From the above results of XANES of each sample, we can determine that the variation of local structure of aluminum oxide with calcinations temperature, and the influence of local structure of aluminum oxide on the electrochemical performances of graphite can be observed in Fig. 2. In Fig. 2 shows the charge-discharge profiles of pristine and Al-treated graphite samples, which calcined 300 and 500°C, during the first cycle and 30th cycle at current density is 350mA/g and cut-off voltage is 0.0-2.5V. Comparing the profiles of the potential curves of Al-treated sample with those of pristine sample, we could not observe the remarkable changes in electrochemical reactions from initial profiles. However, Fig. 2 clearly indicates that the cycle performance was improved by the Al-treatment and calcination temperature.

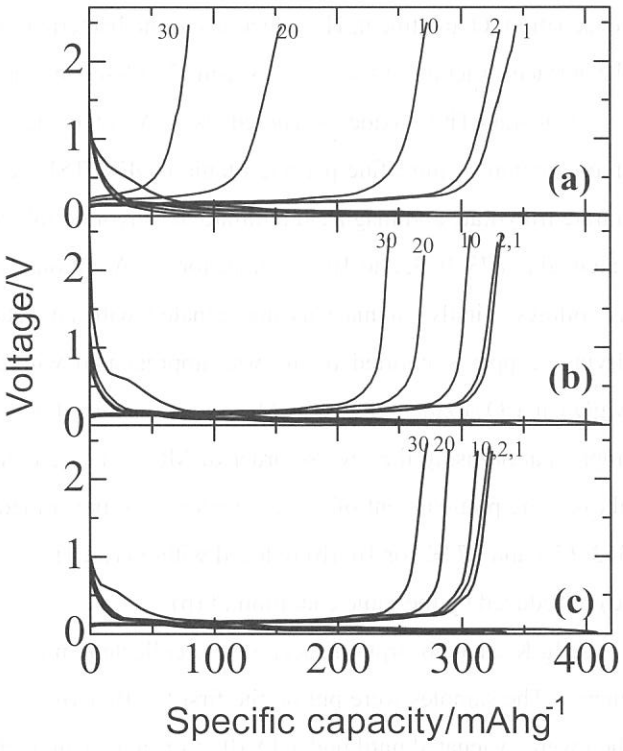

Fig.2. Voltage profile of 1,2,10,20,30th cycle of (a)pristine, (b)Al-treated (calcined at 300℃) and (c)Al-treated(calcined at 500℃) natural graphite electrode.

Refedences

[1] K.Shimizu, Y.Kato, T.Yoshida, H.Yoshida, A.Satsuma and T.Hattori, *Chem. Commun.*,**1999**, 1681 (1999).

(BL7A)

Mg K-edge XANES study of Cu-MgO/TiO_2 oxide for bactericidal materials

Tomomi Kosaka, Ayano Yamada, Yoko Hayashi and Sadao Hasegawa

Department of Chemistry, Tokyo Gakugei University, Koganei, Tokyo, 184-8501

Recently, many inorganic oxides (Ag-zeolite, Zn-hydroxyapatite, TiO_2...and so on) for bactericidal material were developed and investigated by the researchers of university and industry [1~3]. The mechanism of bactericidal effects was suggested as follows. ①The inhibition effect of noble metal ion(Ag^+, Cu^{2+}, Zn^{2+}...that is "Soft acid") which was dissolved from the materials to SH group of enzyme. ②The strong oxidation property of active oxygen species (hydroxyl radical, super oxide, hydrogen peroxide), was produced on the surface of materials under photo irradiation in the case of semiconductor oxide. However, its detailed explanation was still unclear and both suggestions were reliable. In our previous study[4], we prepared TiO_2-SiO_2-MgO tertiary oxide and investigated the OH radicals formation on that of surface contacted with water using the spin-trapping method. In the following experiment, we also investigated the effect of evacuation temperature to OH radical formation. The thermally reduced surface was formed on the TiO_2-SiO_2-MgO oxide by the evacuation at high temperature (over 773K) and the formation of OH radicals was increased. However, the stable electron state was formed by the thermally reduction (Cu^{2+}→Cu^+ or Cu^0) in the case of TiO_2-SiO_2-CuO. The quantity of active oxygen species was decreased by the results of the inhibition of hydrogen abstraction reaction. From these findings and background, we prepared Cu-MgO/TiO_2 oxides and investigated the effects of pretreatment (evacuation, O_2 treatment, H_2 reduction) to the bactericidal function in progress. In this report, we investigated the surface structure of these oxides using Mg K-edge X-ray Absorption Near Edge Structure analysis.

Cu-MgO/TiO_2 oxides (denoted as C-M/T) containing 25wt% Cu and 25wt% Mg were prepared by impregnation of ultra fine particle titania (IDEMITSU KOSAN, IT-S) with an aqueous solution of copper(Ⅱ) nitrate trihydrate and magnesium nitrate hexahydrate followed by drying in air at 383K for 24h. Then, they were calcined at 873, 973, and 1073K in air for 1h. Additionally, we also prepared two different kinds of these oxides as follows. Firstly, titania was impregnated with an aqueous solution of copper(Ⅱ) nitrate trihydrate. After drying, copper supported titania was impregnated with a magnesium nitrate hexahydrate solution, and then MgO/Cu/TiO_2 oxide(denoted as MC/T) was obtained. Cu/MgO/TiO_2 oxide (denoted as CM/T) was prepared by impregnation using the reverse order of MC/T. These oxides were calcined at the same temperature mentioned above. The pretreatment of these samples were performed in a vacuum cell: the samples were (a) evacuated at 383, 673 and 773K for 1h, (b) reduced with 50Torr H_2 for 1h at 473K, (c) oxidized in 50Torr O_2 for 1h at 473K, (d) re-reduced by the same condition of (b).

Mg K-edge absorption spectra were collected on the BL-7A facility at UVSOR, IMS with 750MeV of ring energy. The samples were put on the first Cu-Be dynode of electron multiplier using adhesive carbon tape, and then were evacuated until under $1X10^{-7}$ torr in a vacuum chamber. The spectrum was recorded in a total electron yield mode at room temperature using $KTiPO_4$ [KTP](011) double crystal monochromator (2d=10.954nm).

Mg K-edge XANES spectra of reference samples and MgO/TiO_2 calcined at 873 and 1073K(previous data)

[5] were shown in Fig.1. Fig.2 was also indicated that those of prepared samples (C-M/T, CM/T and MC/T) at various temperatures. It was found that the formation of $MgTiO_3$ was inhibited by Cu addition and 6-fold coordinated Mg (rock salt type structure) predominantly existed in all prepared samples. These results were corresponded to our previous data[5]. However, the characteristic difference of the spectra was detected in the samples calcined at under than 973K. Relative intensity of the peak around 1306eV in CM/T was more weaken than those of the other samples. It was indicated that the environmental structure of Mg was affected by the preparation and the effect of Cu addition was varied by the supporting method. Unfortunately, the effects of pretreatment to the XANES spectra were not shown in this experiment. The mechanism of bactericidal materials was so complex, theoretical and experimental efforts were more need. We believed that XAFS analysis was effective method to clarify this problem.

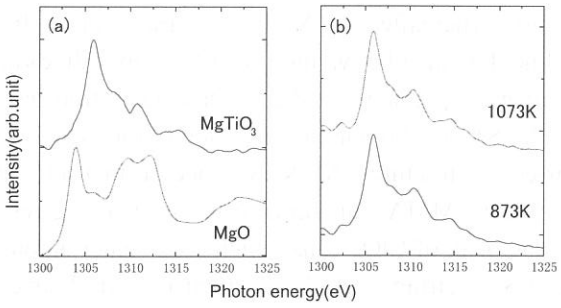

Fig.1 Mg K-edge XANES spectra of (a) reference samples and (b) 25wt% MgO supported titania

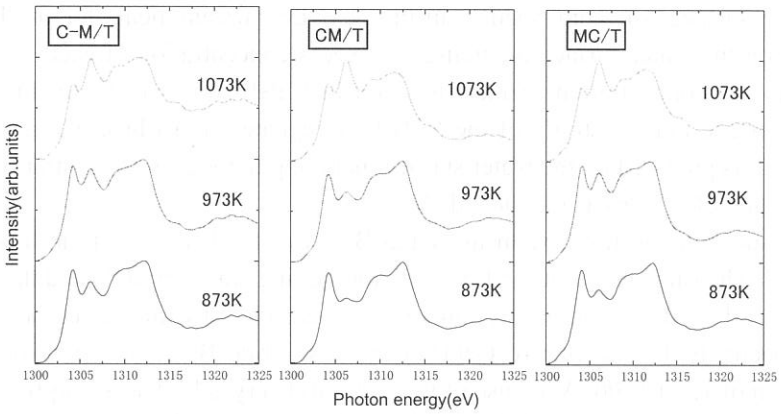

Fig.2 Mg K-edge XANES spectra of Cu and MgO supported titania

Acknowledgements

This work was supported by Grant-in-Aid for Scientific Research (S.H. and T.K.) from Ministry of Education, Culture, Sports, Science and Technology of Japan. T.K. also appreciated to INAMORI foundation.

References

[1] H.Kourai, Y.Manabe, Y.Yamada, J. Antibact. Antifung. Agents, **22**(10),(1994)595.

[2] Q.L.Feng, T.N.Kim, J.Wu, E.S.Park, J.O.Kim, D.Y.Lim and F.Z.Cui, Thin Solid Films, **335**(1998)214.

[3] Y.Kikuchi, K.Sunada, T.Iyoda, K.Hashimoto and A.Fujishima, J.Photochem.Photobiol.A:Chem., **106**(1997)51.

[4] A.Ikuo, M.Takagi, N.Kabasawa, Y.Yoshinaga, S.Teratani and S.Hasegawa, Appl.Surf.Sci., **121/122**(1997)513.

[5] T.Kosaka, A.Yamada, A.Miyaji, M.Shiraishi, and S.Hasegawa, UVSOR activity report 2000, 162.

(BL7A)

Characterization on the Surface of Polymer Ultra Thin Films Impregnated with Ruthenium-Polybipyridine Complex by XAS

Shuji MATSUO[1*], Tsutomu KURISAKI[2], Hisao YAMASHIGE[2], and Hisanobu WAKITA[1,2]

[1]*Advanced Materials Institute, Fukuoka University, Nanakuma, Jonan-ku, Fukuoka 814-0180, Japan*
[2]*Department of Chemistry, Faculty of Science, Fukuoka University, Nanakuma, Jonan-ku, Fukuoka 814-0180, Japan*

*Corresponding author: mashu23@hotmail.com

Poly(methyl methacrylate) (hereafter, PMMA) ultra thin films impregnated with (N,N′-di(hexadecyl)-2,2′-bipyridine-4,4′-dicarboxyamide)-bis(2,2′-bipyridine)ruthenium(II) diperchlorate complex (denoted as RuBP) have been prepared, and the characterization has been investigated by the X-ray absorption spectroscopy (XAS) [1]. So far, it was found from Ru L_3-edge, Cl K-edge, and Br L_3-edge X-ray absorption near-edge structure (XANES) spectra that (1) the RuBP complexes are impregnated only a single-side of the PMMA thin film, resulting that it gives hydrophilicity due to the RuBP complexes; (2) the Cl K-edge peak of ClO_4^- ions which are counter anions in RuBP complex is also observed in the Ru L_3-edge XANES spectrum; and (3) the intensity ratio between the peaks of Cl K-edge and Ru L_3-edge changes in the film-prepared conditions on the water surface, suggested that the surface of the RuBP-impregnated thin film chooses the anion on a water surface, for example ClO_4^- and OH^- ions. The ion-selectivity of the surface was confirmed from the XANES measurements for the RuBP-impregnated thin films prepared on the water surface including the excess concentration of each of ClO_4^-, Cl^-, and Br^- ions, compared with the concentration of the ClO_4^- ion in RuBP solution [2]. In this study, in order to investigate further surface ion-selectivity of the RuBP-impregnated thin films, we measured the XANES spectra for the thin films prepared on the water surface including the excess concentration of each of BrO_3^-, SO_4^{2-}, SO_3^{2-}, $S_2O_3^{2-}$, and SCN^- ions as mentioned above.

The X-ray absorption spectra were measured at BL7A of the UVSOR in the Institute of Molecular Science, Okazaki [3]. The ring energy of the UVSOR storage ring was 750 MeV and the stored current was 110–230 mA. S K- and Ru $L_{2,3}$-edge absorption spectra were recorded in the regions of 2420-2540 and 2800-3000 eV, respectively, by use of two Ge(111) crystals, while Br $L_{2,3}$-edge absorption spectra were recorded in the region of 1550-1700 eV by use of two KTP(011) crystals. The absorption was monitored by the total electron yield using a photomultiplier. The RuBP solution and RuBP-impregnated polymer thin film were prepared by the procedure as described elsewhere [1,4], here, each anion was in advance added to water. These anions were added as sodium salt, and the molar quantity of these anions was 50000 times that in the RuBP solution normally dropped on the water surface. The thin films were directly attached to carbon adhesive sheets, and the reference materials, for example powder of each sodium salt, were spread on the sheets. Each sheet was adhered to the first dynode of the photomultiplier.

The Ru L_3-edge XANES spectra for the RuBP-impregnated thin films prepared on the water surface including the excess concentration of each of BrO_3^-, SO_4^{2-}, SO_3^{2-}, $S_2O_3^{2-}$, and SCN^- ions are shown in Fig. 1 along with that of the RuBP powder and normal RuBP-impregnated thin film. The photon energy is calibrated by setting the Ru L_3-edge peak of the Ru metal to 2838.0 eV. The spectra are normalized to the Ru L_2-edge peak. In all the thin films, no peak A assigned to the Cl K-edge of ClO_4^- ion appears in the XANES spectra, though it appears in those of the RuBP powder and normal RuBP-impregnated thin film. This result suggests that few ClO_4^- ions exist at the RuBP-impregnated surface of the thin film, and another anion interacts with that instead. The S K-edge and Br L_3-edge XANES spectra for those thin films are

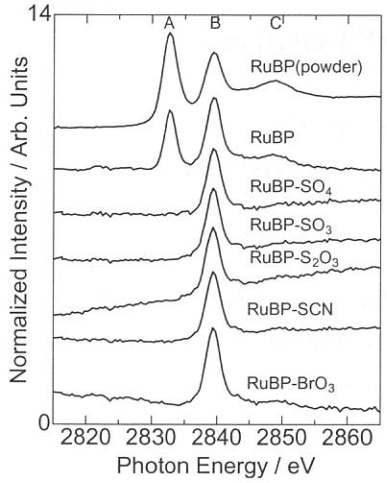

Fig. 1. Ru L_3-edge XANES spectra.

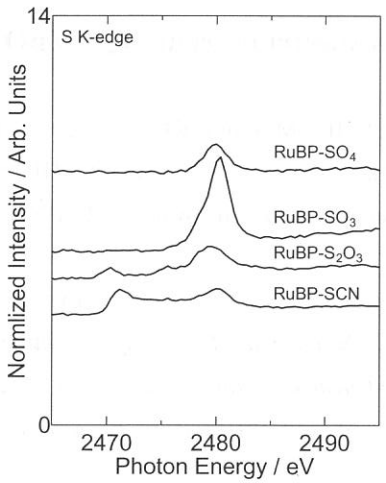

Fig. 2. S K-edge XANES spectra.

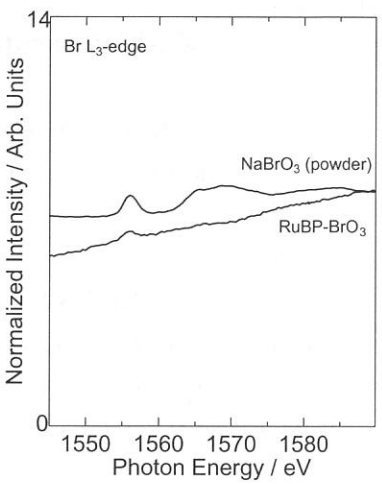

Fig. 3. Br L_3-edge XANES spectra.

shown in Figs. 2 and 3. The XANES spectra for the sodium salts of the S compounds as reference samples are presented in Fig. 4, and that of $NaBrO_3$ is also depicted in Fig. 3. The photon energy for the S K-edge and Br L_3-edge is calibrated by the references of Refs. 5 and 6, respectively. The spectra in Figs. 2 and 3 (only RuBP-BrO_3) are multiplied by the coefficient when the Ru $L_{2,3}$-edge XANES spectra are normalized to the Ru L_2-edge peak, that is, their spectra is comparable in the intensity with that of the Ru L_3-edge. In Figs. 2 and 3, all the anions exist as counter ions at the RuBP-impregnated surfaces of the thin films, though the peak intensity for the ClO_4^- ion in the normal RuBP-impregnated thin film is larger than that of all the anions except for RuBP-SO_3. The RuBP-impregnated surfaces of the thin films may be thus suggested to predominantly interact with another anion rather than BrO_3^-, SO_4^{2-}, $S_2O_3^{2-}$, and SCN^- ions. However, it is not understood why the SO_3^{2-} ions are predominantly adsorbed to the RuBP-impregnated surfaces of the thin film, compared with the other anions, and the peak positions (2480 eV) of RuBP-SO_3, -S_2O_3, and -SCN are similar to that of RuBP-SO_4, though the feature characteristic of each spectrum for RuBP-SO_3, -S_2O_3, and -SCN still remain. This will be clarified by progressing this study furthermore. In conclusion, it is found that the chemical state of the RuBP-impregnated surfaces of the thin film changes by anion added in advance to water.

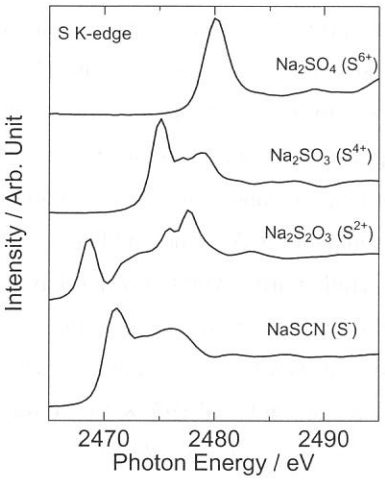

Fig. 4. The S K-edge XANES spectra for the sodium salts of the S compounds as reference samples

This study is supported by the Advanced Materials Institute of Fukuoka University.

References

[1] S. Matsuo, T. Nakano, S. Yamada, T. Matsuo, and H. Wakita, *J. Electron Spectrosc. Relat. Phenom.*, **113**, 193 (2001).

[2] S. Matsuo, S. Yamada, T. Matsuo, and H. Wakita, *Anal. Sci.*, (2002) *in press*.

[3] T. Murata, T. Matsukawa, S. Naoè, T. Horigome, O. Matsuodo, and M. Watanabe, *Rev. Sci. Instrum.*, **63** 1309 (1992).

[4] S. Yamada, Y. Tanaka, M. Kawazu, and T. Matsuo, *Supramol. Sci.*, **5** 379 (1998).

[5] H. Sekiyama, N. Kosugi, H. Kuroda, and T. Ohta, *Bull. Chem. Soc. Jpn.*, **59**, 575 (1986).

[6] T. Matsukawa, H. Okutani, and T. Kinoshita, *UVSOR Activity Reports*, 140 (1999).

(BL7A)

Zn-L_3 absorption spectrum from MgO-ZnO solid solutions

Teruyasu MIZOGUCHI [A], Masahiro KUNISU [A], Masafumi MATSUI [A],
Isao TANAKA [A], Hirohiko ADACHI [A], Tomoko YOSHIDA [B], Hisao YOSHIDA [C],
Shang-Di MO [D] and Wai-Yim CHING [D]

[A] *Department of Materials Science and Engineering, Kyoto University, Sakyo, Kyoto 606-8501, Japan*
[B] *Center for Integrated Research in Science and Eng., Nagoya University, Nagoya, 464-8603, Japan*
[C] *Department of Applied Chemistry, Nagoya University, Nagoya, 464-8603, Japan*
[D] *Department of Physics, University of Missouri-Kansas City, Kansas City, Missouri 64110-2499, USA*

Ceramic solid solutions are widely used not only for functional materials but also for engineering materials. Properties of the ceramic materials are dramatically changed by the kind of the doped solute. In order to control the properties intelligently, detailed knowledge of local structures around solutes is indispensable. X-ray absorption near edge structure (XANES) and electron energy loss near edge structure (ELNES) are versatile tools to analyze them. In this work, MgO-ZnO solid solutions are investigated by XANES and ELNES with special interests on the local structure around Zn in MgO. In order to interpret the experimental spectra, a first principles band-structure calculations were performed using the orthogonalized linear combination of atomic orbitals (OLCAO) method [1].

High purity MgO powder having rock-salt structure (2000A, Ube Materials Industries, Japan) and ZnO powder having wurzite structure (Seido Chemical Corp., Japan) were used as starting materials. Two powders were mixed by a magnetic-starrier in ethanol until they dry up. Sintering was done in air at 1623K for 3h for undoped ZnO, and 1933K for 2h for the doped/undoped MgO. The solubility limit of Zn in MgO was reported to be 38.7 at % at 1873K [2]. All specimens used in this work exhibit a single crystalline phase of a rock-salt structure by a standard powder x-ray diffraction method. XANES was obtained at BL-7A of the soft X-ray beam line of UVSOR, in the Institute for Molecular Science, Okazaki, Japan. Zn-L_3 edge spectra were collected in a total electron yield mode at room temperature using a beryl two-crystal monochrometer. The photon energy was calibrated at the Al K-edge (1568eV) from the beryl monochrometer. Samples were put on the first photocathode of electron multiplier by adhesive carbon tape. ELNES was measured using transmission electron microscopy (CM200 FEG Philips) operated at 200 kV with standard transmission geometry. A post-column imaging filter system (GIF, Gatan) with a slow-scan CCD camera was used in a spectroscopic mode.

Figure1 shows Zn-L_3 ELNES and XANES from wurzite-ZnO (w-ZnO). Two experimental spectra are in good agreement except for the fact that the present XANES shows higher energy resolution than that of the ELNES. As a result, fine structures of peaks A and B can be clearly seen only in the XANES. The theoretical spectrum obtained by the OLCAO method using a large supercell composed of 108 atoms is also shown in Fig. 1. Theoretical spectrum is found to reproduce the experimental spectra quantitatively well up to the peak C if we correct the absolute energy by 15 eV (1.4 %).

Figure 2 shows the Zn-L_3 XANES from the MgO-30mol% ZnO solid solution. The spectral features are clearly different from that of w-ZnO. The spectrum from w-ZnO is basically composed of 4-sets of peaks, A, B, C, and D. On the other hand, the 3-sets of peaks, A, B, and C, make the spectrum from the solid solution. The spectral difference can be ascribed to the difference of coordination number of Zn [3]. The calculated spectrum from an isolated Zn model is also shown in Fig. 2. The isolated Zn model was made up with the assumption that

an isolated Zn ion is present in the MgO matrix. The reproduction of the theoretical spectrum is satisfactory except for small discrepancy in the shape of the peak B. Although the peak B in the experimental spectrum is rather sharp, it shows a double peak in the isolated Zn model. The isolated Zn model should therefore be modified.

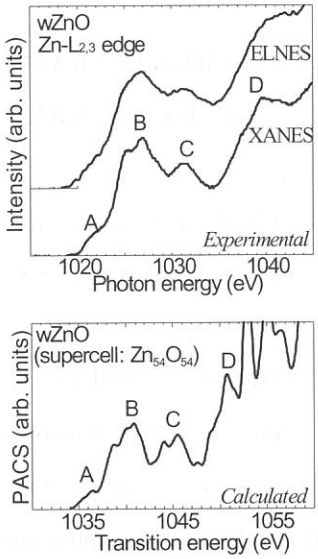

Fig. 1
(top) Zn-L_3 ELNES/XANES from w-ZnO and (bottom) the calculated spectrum by the OLCAO method using a large supercell composed of 108 atoms.

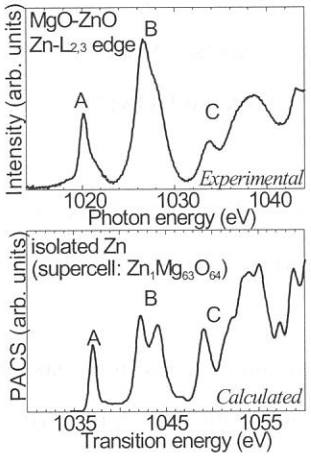

Fig. 2
(top) Zn-L_3 XANES from a MgO-30 mol % ZnO solid solution and (bottom) the calculated spectrum with the isolated Zn model using a $Zn_1Mg_{63}O_{64}$ supercell.

Figure 3 shows the dependency on Zn concentration for the Zn-L_3 XANES. Although the spectral features gradually change depending on the Zn-concentration, the change is not so significant. The doubled peak B found in the theoretical spectrum by the isolated-Zn model did not appear even in the 2.5%Zn specimen. This implies that the isolated-Zn model cannot be applied to the 2.5%Zn specimen, either. This is suggestive of the solute distribution far from random. Strong interaction among Zn atoms in the solid solution should occur even in the low-doped sample.

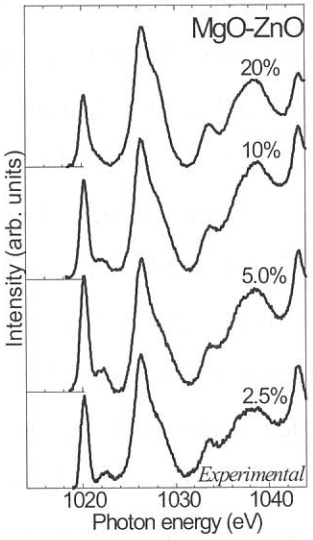

Fig. 3
Dependency on Zn concentration for the Zn-L_3 XANES.

REFERENCES

[1] S. D. Mo and W. Y. Ching, Phys. Rev. B. **62** (2000) 7901.

[2] E. R. Segnit, S. E. Hlland, J. Am. Ceram. Soc., **8** (1965) 409.

[3] T. Mizoguchi, M. Yoshiya, J. Li, F. Oba, I. Tanaka, and H. Adachi, Ultramicroscopy **86** (2001) 363.

(BL7A)

Microstructural control of calcium titanates with some oxides as a dopant and analysis of their local structure by Ca K- and P K-edge XAFS

Atsushi NAKAHIRA,* Ken-ichiro EGUCHI,* Chikako KARATANI,*
Yukako HONDA,* Takayuki MURAKAMI,* and Hirofumi ARITANI**

*Faculty of Engineering & Design, Kyoto Institute of Technology, Kyoto 606-8585, Japan
**Faculty of Engineering, Saitama Institute of Technology, Okabe, Saitama 369-0293, Japan

Calcium titanate, $CaTiO_3$, has the perovskite type structure as well as $BaTiO_3$ for ferroelectric materials. $CaTiO_3$ with the addition of some oxides as a doping is expected to possess the possibility of novel ferroelectric properties. Recently, according to Hayakawa et al, it was also reported that the usage of $CaTiO_3$ based materials with small amount of nickel led the exothermic reaction without H_2O in the case of the oxidation of methane. In this study, the evaluation of microstructure for $CaTiO_3$ with the addition of some oxides and its structural analysis around Ca and P atoms was carried out by means of Ca K- and P K-edge XAFS. In this report, obtained results and discussions about P K-edge XAFS were omitted.

As an initial material, $CaTiO_3$ powder, zirconium oxide powder, strontium oxide powder, and barium nitrate were selected. 5 wt% of their oxide powders and salt was added into $CaTiO_3$ powder and mixed in ethanol solvent for 24 hours by a ball-milling method. The slurry was dried with an evaporator and then in an oven at 50℃. The mixture of $CaTiO_3$ and other oxides or salt was molded with a stainless die. The compacts were heat-treated in an air atmosphere for 2 hours at 1100 - 1300°C. XAFS spectra at Ca K- and P K-edges were measured at BL7A of UVSOR by means of Ge(111) double-crystal monochromator. All samples were measured in a total electron yield mode.

Heat-treated $CaTiO_3$ with some additives was identified by X-ray diffraction (XRD) and composed of only $CaTiO_3$ phase without reaction phases. The XRD results indicated that these $CaTiO_3$ with some additives had the perovskite-type structure. It is suggested that the solid solution of Ba, Zr, and Sr into $CaTiO_3$ structure was performed. Fig. 1 shows XANES spectra of $CaTiO_3$ with some additives. $CaTiO_3$ has perovskite-type orthorhombic structure, and Ca ions are surrounded by 12 oxygen atoms in three types of slightly distorted square-planner CaO_4 tetrahedra. Thus the feature of XANES are quite different from those of CaO (CaO_6, O_h) and HAp (Ca-O_{10}). In case of $CaTiO_3$ with several additives (Sr, Ba, Zr, or La), the features of XANES spectra are almost similar to that of non-doped $CaTiO_3$. However, the transition intensities of each peak (especially, prominent peak at 4044 eV) on these samples have a little difference from each other. This result indicates that a little change was brought about in Ca local structure by addition of those dopants. Fig. 2 shows EXAFS oscillation waves of these samples in the range of Δk = 3.0 - 10.0

$Å^{-1}$. Slight difference of oscillations can be between $CaTiO_3$ and Ba-, La, or Zr-added one, supporting the structural change around Ca ions in minor. To clarify the difference, Fourier-transformed EXAFS analysis was introduced. The results of FT are shown in Fig. 3. In $CaTiO_3$, two types of Ca-O bonds are present in the range of 2.39 - 2.50 (8O) and 2.58 - 2.69 Å (4O). For FT-EXAFS, it seems that Ca-O scattering of these bonds are seen in the range of R = 2.2 - 3.2 Å (as shoulder and primary peaks). The FT peak at ca. 4.0 Å may be due to Ca-Ti scattering (3.84 Å as a real bond length). The feature of Ca-O peaks in 5wt% Sr-added $CaTiO_3$ is almost as same as those of $CaTiO_3$, however, the difference can be seen in 10wt% Sr-added $CaTiO_3$ from non-doped one. In addition, intensity of the peaks in higher shells ($R \geq 4.0$ Å) becomes large by Sr addition. These results show that Sr-insertion in $CaTiO_3$ perovskite give a successive change of local structure around Ca ions in minor. In cases of La- or Zr-added $CaTiO_3$, separate peaks due to Ca-O scattering can be seen at 2.4 and 3.3 Å. The peaks at 4.2 Å, which may be due to overlapped Ca-La or Ca-Zr scattering with Ca-Ti one, becomes large by metal-addition. These change of local structure around Ca ions in $CaTiO_3$ perovskite phase. The slight change of Ca local structure.

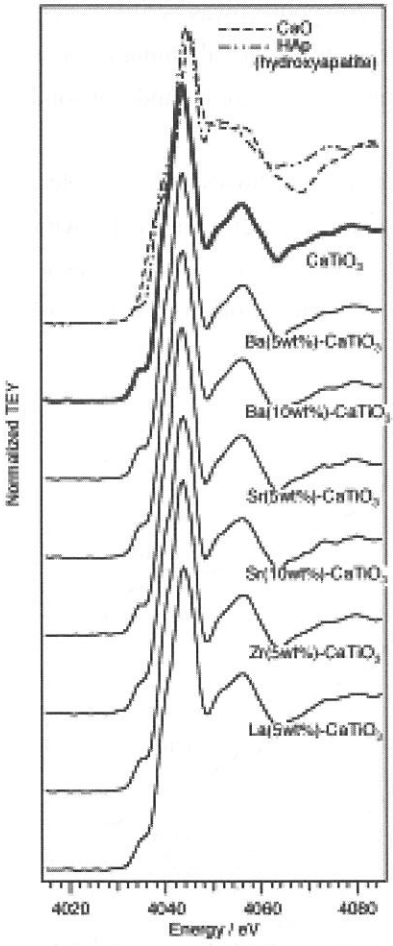

Fig. 1 Ca K-edge XANES.

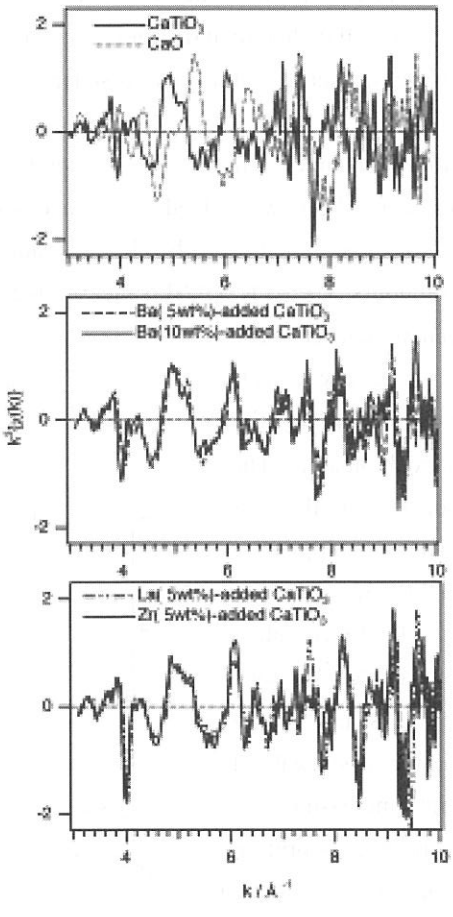

Fig. 2 EXAFS oscillations.

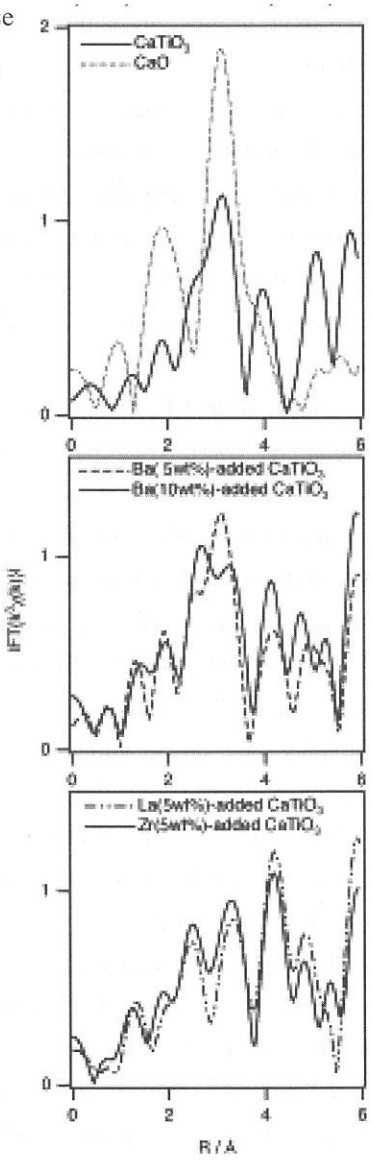

Fig. 3 FT-EXAFS (Δk=3-10).

(BL-7A)

An Electronic Study on the Analysis of Al K X-ray Absorption Near Edge Structure for on Aluminum Adsorbed Ion-exchange Resin

K. Shirozu[1], S. Matsuo[2], T. Kurisaki[1], T. Yokoyama[3], and H. Wakita[1,2]

[1]*Department of Chemistry, Faculty of Science Fukuoka University*
Nanakuma, Jonan-ku, Fukuoka 814-0180, Japan
[2] *Advanced Materials Institute, Fukuoka University*
Nanakuma, Jonan-ku, Fukuoka 814-0180, Japan
[3]*Department of Chemistry, Faculty of Science Kyushu University*
Hakozaki, Higashi-ku, Fukuoka 812-8581, Japan

Fulvic acid is a typical organic compound with aliphatic and/or aromatic carboxylic and phenolic hydroxyl groups in natural water. It is also a polymer which has molecular weight of 1000-10000. Therefore, it is important to understanding the behavior of aluminum ion with this acid on the environmental science. Thus for understanding the binding properties of aluminum ion to fulvic acid, it is also important to investigate the interaction between aluminum ion and some model compounds of fulvic acid that have functional groups such as carboxylic groups and amino groups in aqueous solution. We choose a chelate and cation exchange resin. But the structure of these model compounds was not clear yet. In this study, the Al K XANES spectra of the chelate and cation exchange resin adsorbing aluminum ion as model compounds for fulvic acid were measured and discussed steric structure of these compounds in solid state.

Chelate resin, Chelex 100, and cation exchange resin, Bio-Rex 70, were obtained from Bio-Rad Laboratories, Richmond, Calif., respectively. Each resin (2-5g) was added into aqueous solutions (100-200 cm^3, pH3) with various concentrations of aluminum ions and stirred for 24h. The resin adsorbing aluminum ions was filtered, air-dried and dried at 60°C for several hours. The Al K XANES measurements were carried out at the BL-7A of UV-SOR in the Institute for Molecular Science. The storage ring was operating at electron energy of 750 MeV. All spectra were recorded in total electron yield, using a KTP double-crystal monochromator. The samples were spread into the carbon film on the first photodynode made of CuBe of the electron multiplier.

Fig.1 shows Al K XANES spectra of the resin adsorbing aluminum ions and Al(CyDTA) complex. Al(CyDTA) complex contains six coordinated Al^{3+} ions, each of which is bonded to two N atoms and four O atoms. For Al K XANES spectra, the first peak of K-edge shifts higher energy with increasing the coordination number of aluminum ions. The absorption edges of the three compounds are located on the same energy level. The result shows that these compounds have similar surroundings of aluminum ions.

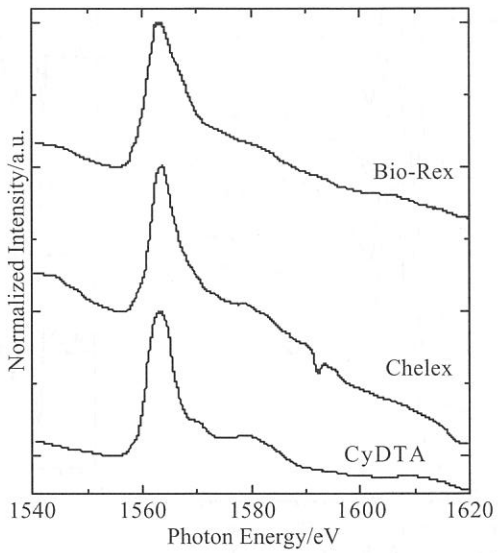

Fig. 1 Al K XANES spectra of the resin adsorbing aluminum ions and Al(CyDTA) complex

(BL8B2)

Ultraviolet Photoelectron Spectra of Surface Lattice Oxygen of $LiNiO_2$

T. Miyazaki[1], D. Yoshimura[2], K. Kamiya[2] and Yamaguchi[1]

[1] *Department of Applied Chemistry, Faculty of Engineering, Ehime University, Matsuyama, 790-8577*

[2] *Institutes for Molecular Science, Okazaki, 444-8585*

Several metal oxides have been utilized as catalysts of the oxidative coupling of methane (OCM). $LiNiO_2$ has an activity for the OCM reaction and a layered structure in which lithium and transition metal ions are alternately and regularly arranged to oxygen layers. We suggested that the anisotropic structure should be a key to the formation of the active sites for the OCM reaction. In this study, ultraviolet photoelectron spectra (UPS) were measured in order to examine electronic structures of the valence band of $LiNiO_2$. It should be carefully investigated, because the top of the valence band usually determines chemical activities and properties.

The measurements of ultraviolet photoelectron spectra were carried out at the BL8B2 of the UVSOR/IMS. $LiNiO_2$ was synthesized by solid phase reaction at 800℃ in the atmosphere. The surface treatments were carried out by a surface cutting under high vacuum and/or argon sputter. The $h\nu$-dependence of ultraviolet photoelectron spectra of $LiNiO_2$ was also measured at room temperature.

Ultraviolet photoelectron spectra of $LiNiO_2$ after the surface treatment are shown in Figs. 1 and 2. These spectra were measured with reference to E_F as zero of the energy scale. Fig. 1 is different demonstrating the effect of the surface contamination and/or modification by air. Fig. 2 shows the incident photon energy dependence of UPS of $LiNiO_2$. The intensity of these bands at E_b=6.9 eV and E_b=1.6, 2.7, 3.5 eV from the Fermi level shows maximum at around $h\nu$=40 eV and 55 eV, respectively. It seems likely to be a considerable possibility of orbital mixing between Li, Ni and O atoms.

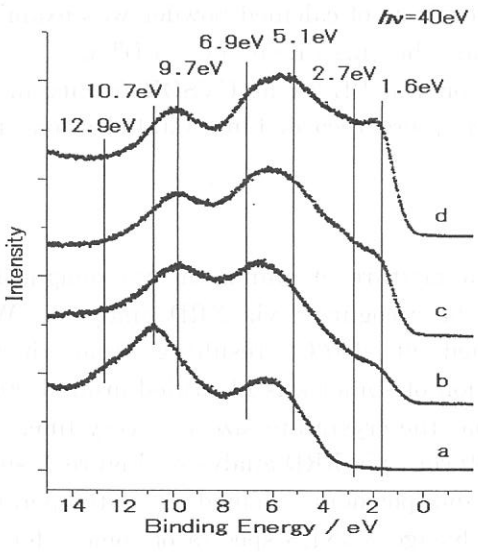

Fig.1. UPS of $LiNiO_2$, a) $LiNiO_2$ sample of no surface treatment; b)-d) $LiNiO_2$ sample after the surface cutting and argon sputter treatments.

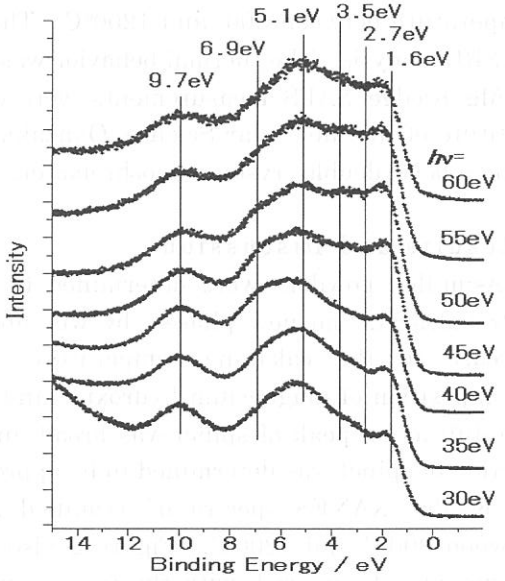

Fig.2. The $h\nu$-dependence of UPS of $LiNiO_2$ in the $h\nu$-region of 30 - 60 eV.

(BL7A)

Mg K-Edge XANES Study of Crystallization of $MgAl_2O_4$ Spinel Prepared from A Mixture of $Al(OH)_3$ and $Mg(OH)_2$ Activated Mechanically by Wet Milling

Takeshi SHIONO, Takushi MINAGI, Hirofumi ARITANI
Shinya OKUMURA and Toshihiko NISHIDA

Department of Chemistry and Materials Technology
Kyoto Institute of Technology
Matsugasaki, Sakyo-ku, Kyoto, 606-8585, Japan

1 Introduction

$MgAl_2O_4$ spinel is recognized as one of structural oxide materials because of high melting point (2015°C), superior resistance to chemical attacks strength and so on. However, it is very difficult to prepare dense polycrystalline spinel with high-purity and stoichiometric composition by a conventional method. Advanced synthesizing techniques have been applied to preparation of the powder with good sinterability[1-3]. Mechanochemical process is a well-known process that improves the reactivity of powders and gives new properties to them, using mechanical stress by agitating and milling processes. Despite mechanochemical phenomena are applied to various industrial fields in practice, few studies of quantitative mechanochemistry were carried out.

In the present study, the formation of spinel phase from a mixture of aluminum and magnesium hydroxide activated mechanically with wet-milling was investigated through X-ray diffraction (XRD) analysis and Mg K-edge X-ray near-edge structure (XANES).

2 Experimental

Aluminum hydroxide (Sumitomo Chemical Industries Co. Ltd. : C-31) and magnesium hydroxide (Ube Chemicals Co. Ltd. : UD-653) was used as raw materials for mechanical milling, without further heat treatment and purification. The average particles size were 50μm and 2.8μm respectively. For preparation of activated powder, the hydroxides were milled in hydrochloric solution with a Mg : HCl molar ratio of 1 : 0.01 by using a planetary ball-milling equipment (Fritsch Co. Ltd. : P-5). The milled hydroxide powders were calcined at a temperature between 300° and 1200°C. The crystalline phase of calcined powder was examined via XRD analysis. The thermal behavior was estimated at a heating rate of 5°C via DTA.

Mg K-edge XAFS measurements were carried out on the BL-7A at UVSOR facility in the Institute of the Molecular Science, Okazaki. The spectra were recorded in a total electron yield, using a beryl double crystal monochromater.

3 Results and Discussion

As-milled powders were determined to consist of a mixture of aluminum and magnesium hydroxides and no new phases by wet milling could be recognized via XRD analysis. With increase in the calcining temperature, MgO formed at 600°C, resulting from thermal decomposition of magnesium hydroxide and the formation of spinel was identified around 900°C. The diffraction peak of spinel was broad, indicating that the crystallite size was very fine. The fraction of spinel was determined to be approximately 49 vol% via XRD analysis. Figure 1 shows Mg K-edge XANES spectra of as-milled hydroxide and powders calcined at a temperature between 300°C and 1200°C. Figure 2 also shows Mg K-edge XANES spectra of some reference compounds. Compared with the figures, magnesium element is found to exist as a hydroxide until a calcining temperature of 600°C and formation of MgO could be recognized at 600°C. These results are in good agreement with those by XRD analysis. XANES spectrum at 900°C looks a combination of spectra for spinel and MgO. In order to examine the degree of reaction to

spinel, therefore, we tried to combine the XANES spectra of MgO and spinel in Fig.2, with changing the intensity ratio of each spectrum. Dashed line in Fig.3 shows the result of the combination for 57% MgO and 43% spinel. The combined curve was similar to the spectrum obtained at 900°C, as shown in Fig.1. The fraction of spinel, 43% would be good agreement with the result, 49% from XRD analysis, although the fraction was a little bit smaller.

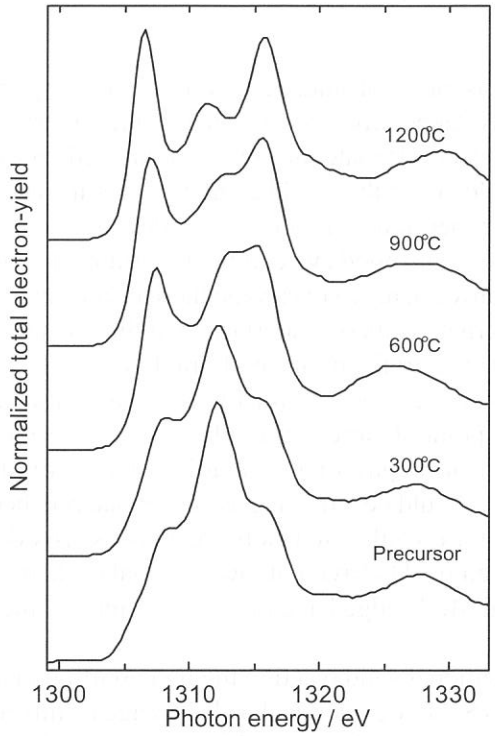

Fig.1. Mg K-edge XANES spectra of spinel precursor and powders.

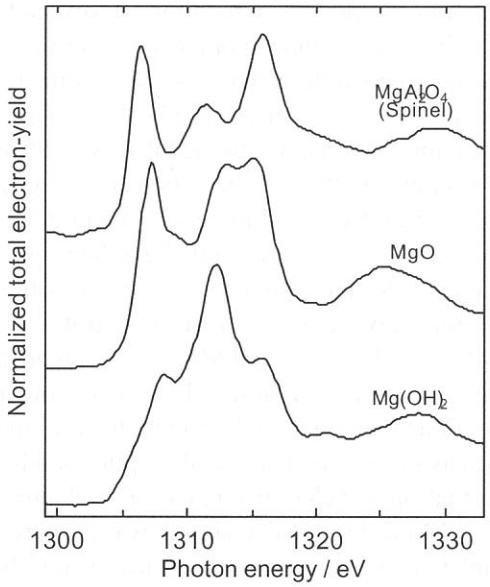

Fig.2 Mg K-edge XANES spectra of reference Mg compounds.

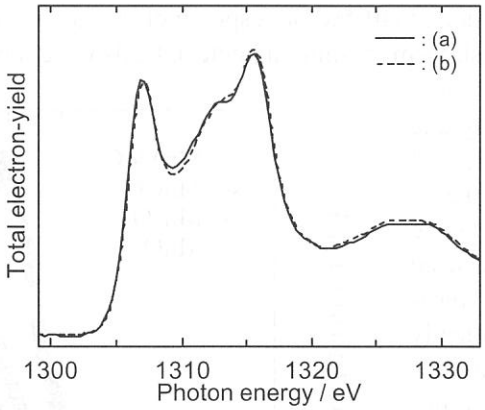

Fig.3. Combination of XANES spectra for spinel and MgO.
(a) spinel powder calcined at 900°C
(b) [spectrum of 57% MgO] + [spectrum of 43% spinel]

References

[1] R.J.Rratton, *J. Am. Ceram. Soc. Bull.*, **48**, 759 (1969).

[2] S.Hokazono, K.Manako and A.Kato, *Br.Ceram.Trans.J.*, **91**, 77 (1992).

[3] T.Shiono, K.Shiono, K.Miyamoto and G.Pezzotti, *J. Am. Ceram. Soc.*, **83**, 235 (2000). the result

(BL7A, BL8B1)

Mo and Mn *L*-XANES of $MnMoO_4$ for high capacity anode material of Li secondary battery

Yoshiharu UCHIMOTO, Seiichiro OGURA, Hiromasa IKUTA, and Masataka WAKIHARA
Department of Applied Chemistry, Graduate School of Science and Engineering, Tokyo Institute of Technology, 2-12-1 Ookayama, Meguro-ku, Tokyo 152-8552, Japan

The Li-ion rechargeable batteries are considered as the most suitable power sources for portable electronic devices due to their high capacity and energy density. Generally, Li-ion rechargeable batteries consist of intercalation compounds in both for cathode and for anode electrode materials. One is a lithiated transition metal oxide as the cathode and the other is graphite as the anode. However, the graphite anode material commonly used in Li-ion rechargeable batteries suffers from small capacity per unit weight (about 350mAh/g) and/or per unit volume due to its low density in spite of its low redox potential and good cycle life. Furthermore the rate capability of graphite material due to the diffusivity also needs improvement. To overcome these disadvantages, considerable amounts of attempts have been made to find out alternative anode materials, including metal oxide(MO, M=Co, Ni, Fe), tin-based material, vanadium-based oxide materials, in place of graphite anodes. Especially, vanadium based oxide materials have been researched as active materials for Li secondary battery, since the vanadium oxides have interesting characteristics in a standpoint of variety of oxidation state. Recently, several researchers have described the low potential Li-insertion behavior in vanadium based oxide such as RVO_4(R=In,Cr,Fe,Al,Y) and MnV_2O_6. Molybdenum oxides should be attractive as anode material, because they also have various oxidation state like vanadium. In this report, we synthesized molybdenum-based oxide $MnMoO_4$ as new anode material and described the lithium insertion/removal behavior at low potential cycle property. The XRD measurement and X-ray absorption study of Mn and Mo L-edge have provided insight on the structural transformation and electrode reaction mechaniam.

$MnMoO_4$ powder sample was prepared by conventional solid reaction method. Starting material used was $MnCO_3$(99.9% Soekawa chemicals) and MoO_3(99.9% Soekawa chemicals). This reagents mixed with stoichiometric ratio in agate mortar and the mixture was heat-treated at 600°C for 24h in air atmosphere. Then we could get crystalline $MnMoO_4$ powdered sample. The phase identification was carried out by powder X-ray diffractometry using Rigaku RINT2500V with CuK¥á radiation. The samples for the electrochemical measurement were prepared by mixing crystalline $MnMoO_4$, acethylene black as conductive agent and polytetraflouroethylene (PTFE) binder(55-40-5wt%, respectively) in an agate mortar and made in the form of film. The film was then cut into a disk form (5.4mm diameter). Cells were fabricated by coupling this disc with lithium foil of same area as counter electrode using microporous polyprophylene film(Celgard2400) as separator. 1M $LiClO_4$ dissolved in Ethylene Carbonate(EC)/DiEthlylene Carbonate(DEC) (vol ratio=1:1) was used as the electrolyte. The electrochemical measurement was carried out galvanostatically at various current densities at room temperature in a glove box under argon atmosphere. The cut-off voltage was set at 0.0 and 2.0V versus Li/Li^+. Mo *L*-edge X-ray Absorption Near Edge Structure (XANES) of synthesized powder were measured on BL7A at UVSOR (Okazaki, Japan) with a ring energy of 750MeV and a stored current of 70-220mA in a mode of total electron yields. The KTP double crystal monochromator was used. The absolute energy scale was calibrated by using literature

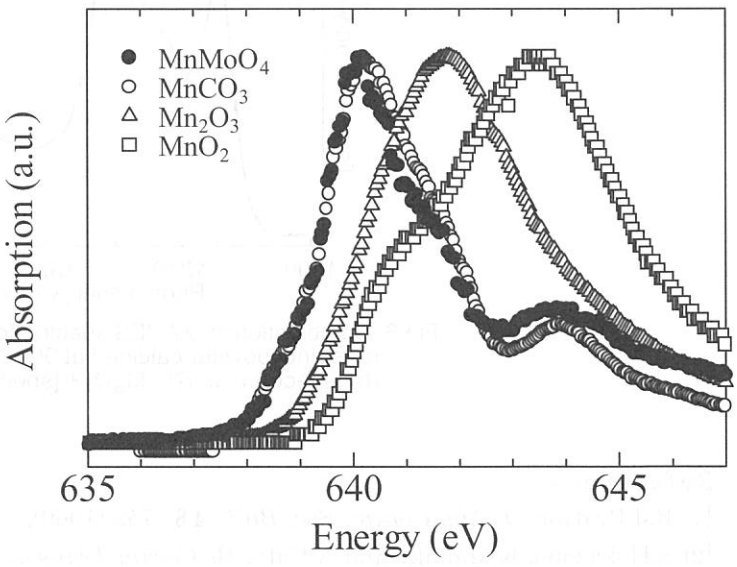

Fig.1. Mn *L*-edge XANES spectrum of $MnMoO_4$ and various Mn compounds as reference

value of Mo L_{23}-edge in MoO_3. Mn L_{23}-edge XANES was measured on BL8B1 beam line at UVSOR (Okazaki, Japan) with ring energy of 750 MeV in a mode of total electron yield at room temperature.

Mn and Mo XANES for synthesized powder also carried out to investigate the oxidation state of Mn and Mo and to verify the chemical formula. XANES results were shown in Fig.1 and Fig. 2 with reference materials that have various oxidation states. The Mn *L*-edge XANES shows two strong absorption features due to the spin-orbit splitting of the Mn 2p core hole. The absorption shown in Fig.1 about 640-645 eV is $2p_{3/2}$ (L3) edge. In Fig.1, the spectra for the edge jumps for $MnCO_3$ and $MnMoO_4$ are very close to each other, we can assume that Mn exists as Mn^{2+} in $MnMoO_4$. Mo L-edge XANES spectra of $MnMoO_4$ and MoO_3 presented in the Fig. 2 illustrate that the valence of Mo in $MnMoO_4$ should be +6. The oxidation state arrived from the XANES spectra and well-defined XRD pattern obtained for the prepared sample confirm that the compound is stoichiometric $MnMoO_4$. Furthermore, the spectra of Mo L-edge XANES of $MnMoO_4$ and MoO_3, which involves the transitions from the 2p core levels into the empty 4d orbital, show separation of two peaks clearly. Generally, in octahedral coordinated metal, the d-orbitals are splits into triply degenerate t_{2g} and doubly degenerate e_g orbitals. The electrons in e_g orbitals are repelled more strongly by the negative charge since electrons are located along the bonding axes than those of t_{2g} orbitals which point between the axes. Thus the t_{2g} orbitals lie lower in energy than the e_g orbitals, whereas, in tetrahedral coordination, triply degenerate t_2 orbitals lie higher in energy than doubly degenerate e orbitals. The Mo atoms in MoO_3 are in a octahedral environment, and Fig.2 indicate the typical 4d splitting in two sets of e_g and t_{2g} symmetry. On the other hand, the Mo atoms in $MnMoO_4$ are in a tetrahedral environment, and Fig.3(b) shows ligand field splitting parameter: (energy difference of t_2 and e) is about 1.6eV.

In order to obtain charge-discharge profile of $MnMoO_4$, cell was subjected to several cycles at constant current mode. The charge-discharge profiles obtained are depicted in Fig. 3. The initial charge capacity was about 1800Ah/kg and reversible capacity in consequent discharge process was around 1000Ah/kg. During the first charge, the lithium intercalation process exhibited a plateau around 0.8V versus Li/Li^+ which is not observed in the following cycles.

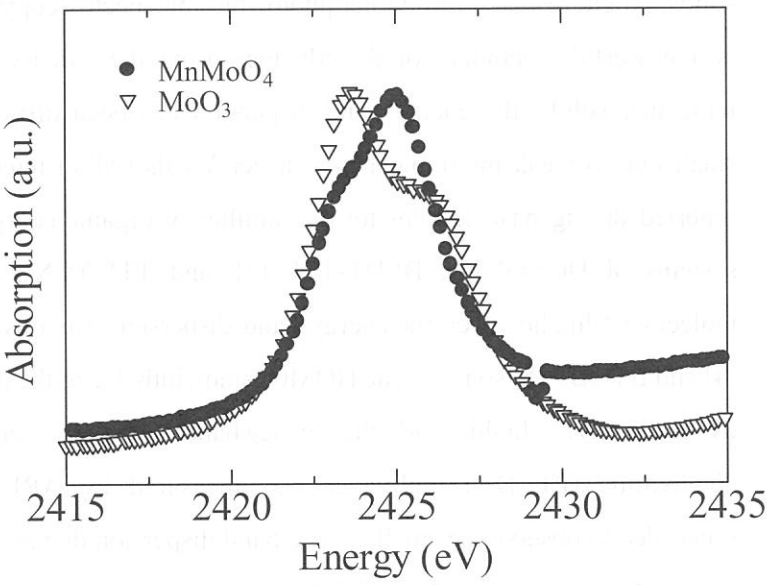

Fig.2. Mo *L*-edge XANES spectrum of $MnMoO_4$ and MoO_3.

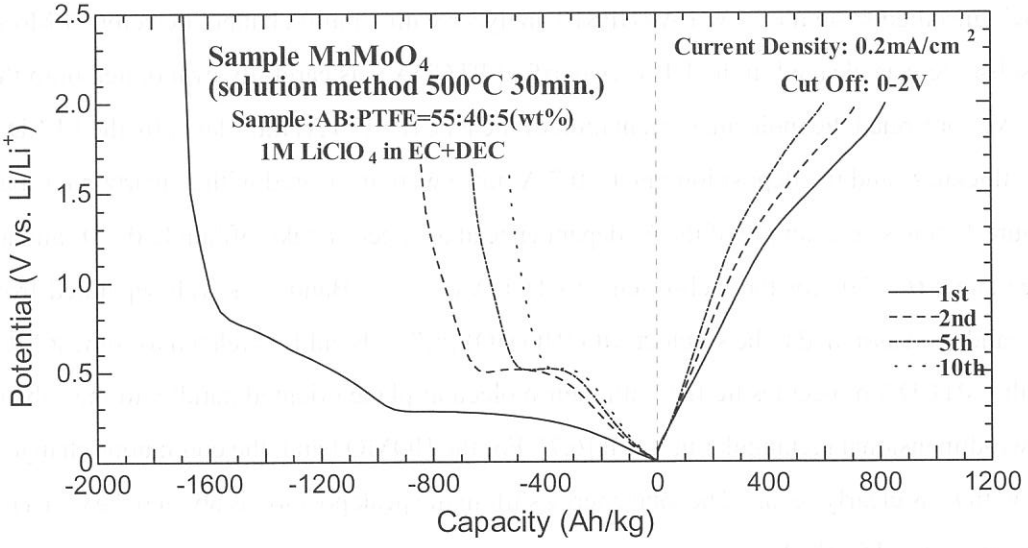

Fig.3 Charge-discharge voltage profile of $MnMoO_4$.

(BL8B2)

Intermolecular Energy-Band Dispersion in Well-Oriented PTCDA Multilayer by Angle-Resolved UV Photoemission

Satoshi KERA[a], Shinji TANAKA[a], Yosuke YABUUCHI[a], Tadaomi MORI[a], Hiroyuki YAMANE[a.b], Daisuke YOSHIMURA[b], Koji K. OKUDAIRA[b], and Nobuo UENO[a]

[a]*Graduated School of Science and Technology, Chiba University, Chiba 263-8522*

[b]*Institute for Molecular Science, Okazaki 444-8585*

The energy-band dispersion is a fundamental basis for understanding the basic properties of solids. Angle-resolved ultraviolet photoemission spectroscopy (ARUPS) using synchrotoron radiation is a powerful technique for directly measuring the valence band dispersion. For typical organic molecular solids, the energy-band dispersion has been difficult to observe, since the bandwidth is small due to weak intermolecular van der Waals (vdW) interaction. Some experiments have been reported during past decades for the families of organic charge transfer salts, such as metal complex systems of DCNQI [1], BEDT-TTF [2], and TTF-TCNQ [3]. In a single-component organic molecular film, however, the energy-band dispersion was observed for only two systems, that is, C_{60} [4] and BTQBT [5] so far. The HOMO bandwidth due to the dispersion is about 0.4 eV for C_{60} and 0.4 eV for BTQBT. In this work, the valence band of well-characterized perylene-3,4,9,10-tetracarboxylic dianhydride (PTCDA) multilayer was measured by ARUPS with synchrotoron radiation. We succeeded to observe the small energy-band dispersion due to the weak HOMO-HOMO interaction for a conventional organic solid PTCDA.

ARUPS measurements were carried out at the BL8B2 of UVSOR. ARUP spectra were measured by a newly installed system of a VG-ARUPS10 analyzer with a multi channel detector. A MoS_2 single crystal substrate was cleaved in the UHV. A purified PTCDA was carefully evaporated onto the MoS_2 surface. We confirmed the molecular orientation of the PTCDA (30 Å) multilayer by the LEED pattern. The film thickness and the deposition rate (~ 0.7 Å/min.) were measured with a quartz microbalance.

Figure 1 shows an example of the *hv* dependence at an electron take-off angle $\theta = 0°$ and a photon incidence angle $\alpha = 70°$ for the well-oriented PTCDA (30 Å). Band A is well separated from other valence bands and assigned to be single π MO (HOMO) [6,7]. Band B is related to some π MOs [6,7]. In this film, PTCDA molecules lie flat with their molecular plane oriented parallel to the substrate and form a two-dimensional rectangular unit cell [6,7]. For the HOMO band, the continuous change of peak position with *hv* is clearly seen. The total energy shift in the peak position is about 0.2 eV in a region of photon energy hv = 15–81 eV.

From Fig.1, the energy band dispersion relation along the surface normal was determined using the procedure described in the previous report [5], where assumed that (i) both energy and momentum of electrons are conserved for the ionization and (ii) the final continuum state is a parabolic free-electron like band in a constant inner potential V_0. In Fig.2, the best fit dispersion curve along with the experimental results calculated by a simple tight-binding model is shown, where inner potential V_0 is –8.5 eV, the binding energy of the band center is 7.43 eV, the lattice spacing is 3.7 Å, and the transfer integral is 0.05 eV. As seen in Fig.2, we could observe the energy-band dispersion over four Brillouin zones (3rd, 4th, 5th and 6th zones) with the bandwidth of about 0.2 eV. For V_0 value, further confirmation is now in progress using the low-energy transmission spectroscopy [8].

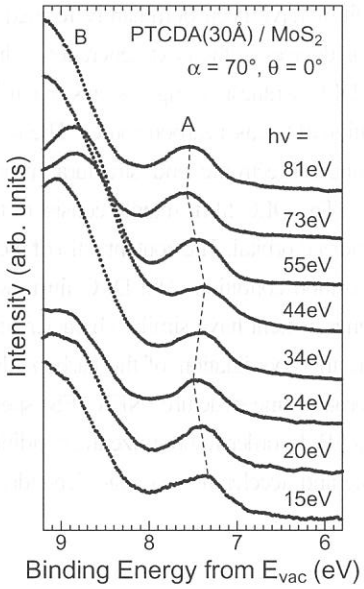

Fig.1 Photon energy dependence of ARUPS at normal emission for PTCDA (30Å) on MoS_2.

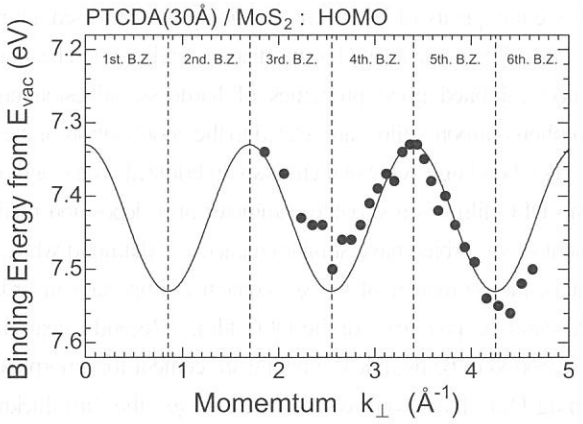

Fig.2 The experimental dispersion for the HOMO band (filled circles) and the best fit curve (line) in the tight-binding model.

[1] For example, D. Schmeisser et al., Solid State Commun. **81**, 827 (1992).

[2] For example, H. Mori et al., Physica C **357-360**, 103 (2001).

[3] For example, F. Zwick et al., Phys. Rev. Lett. **81**, 2974 (1998).

[4] G. Gensterblum et al., Phys. Rev. B **48**, 14756 (1993).

[5] S. Hasegawa et al., J. Chem. Phys. **100**, 6969 (1994).

[6] Y. Azuma et al., J. Appl. Phys. **87**, 766 (2000); J. Synchrotron Rad. **5**, 1044 (1998).

[7] S. Kera et al., Phys. Rev. B **63**, 115204 (2001).

[8] H. Yamane et al., Phys. Rev. B **64**, 113407 (2001).

(BL8B1)

Characterization of the diamond-like carbon films formed by Ar gas cluster ion beam assisted deposition

Teruyuki Kitagawa[1], Kazuhiro Kanda[2], Yutaka Shimizugawa[2], Yuichi Haruyama[2], Shinji Matsui[2], Mititaka Terasawa[1], Harushige Tsubakino[1], Isao Yamada[2,3], Tatsuo Gejo[4] and Masao Kamada[4]

[1] *Himeji Institute for Technology, Faculty of Engineering, Himeji, Hyogo, Japan*
[2] *Himeji Institute for Technology, Laboratory of Advanced Science and Technology for Industry, Kamigori, Hyogo, Japan*
[3] *Collaborative Research Center for Cluster Ion Beam Process Technology, Kyoto University, Sakyo, Kyoto, Japan*
[4] *Institute for Molecular Science, Okazaki, Aichi, Japan.*

Diamond-like carbon (DLC) films have been very interesting material in view of their numerous applications because of their high hardness, low friction coefficient and chemical inertness. DLC films have been dominantly formed by vapor phase methods [1,2], however their properties are not sufficient for the various devices in the next generation. In order to improve the quality of DLC film, our group has proposed a novel method in DLC synthesis using gas cluster ion beam [3]. The DLC films were formed by irradiating Ar cluster ion beam during evaporation of C_{60} as a carbon source. The films by this method exhibited good properties of hardness, adhesion and wear resistance. Electronic and structural properties of amorphous carbon films are related to the coordination of the carbon atoms. The DLC films mainly consist of two phase of carbon bonding. One of them is sp^2 hybridized orbital and other is sp^3 hybridized orbital. The content ratio of these phases in the DLC films is a variable parameter of a deposition method and a deposition condition. The DLC films with lower content of sp^2 orbital have similar character of diamond while those with higher content have similar character of graphite. That is, the estimation of the sp^2 content is important in order to determine the coordination of the carbon film and to understand the properties of the DLC film. Recently, near edge X-ray absorption fine structure (NEXAFS) spectroscopy was reported to be useable estimating sp^2 content for amorphous carbon films [4]. In order to optimize the condition on the forming DLC films with lower content of sp^2, the film thickness dependence and acceleration voltage dependence in the NEXAFS spectra were measured.

NEXAFS measurement was performed at the BL8B1 station of UVSOR [5]. The synchrotron radiation provided by the 0.75 GeV electron storage ring was dispersed by a constant-deviation constant-length spherical grating monochromator and was perpendicularly irradiated to the film surface. The NEXAFS carbon *K*-edge spectra were measured in the photon energy range 275-320 eV with 0.5 eV FWHM resolution. The detection of electrons emitted from sample was performed in the total electron yield mode. The details of the deposition method of DLC film by using GCIB assisted deposition have been described in the previous paper [3]. The accuracy in

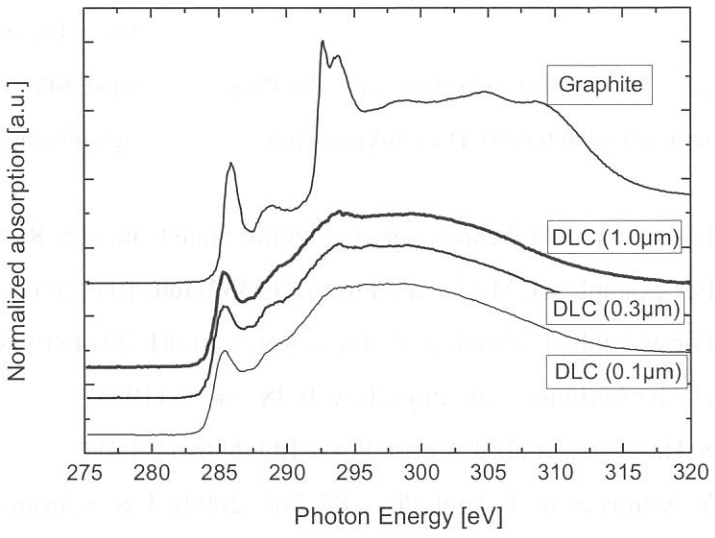

Fig.1 NEXAFS spectra of graphite and DLC films formed by Ar gas cluster ion beam (GCIB) assisted deposition. The films were deposited with various film thicknesses.

our NEXAFS spectra was confirmed by measuring the reference sample of graphite as shown fig. 1.

Fig. 1 shows the typical NEXAFS carbon *K*-edge spectra of the DLC films formed by GCIB assisted deposition with the spectra of graphite. The spectra of DLC films with various film thickness, which were deposited with 9kV acceleration voltage of GCIB, are shown. The NEXAFS spectra of various carbon films have been investigated previously [4,6,7]. A pre-edge resonance at 285.3 eV is due to transitions from C 1*s* level to unoccupied π^* orbital principally originating from sp^2 (C=C) hybridized orbital. This peak is not almost present in the diamond spectrum [8], because the diamond consists of only sp^3 (C-C) orbital. Therefore the intensity of the transitions at 285.3 eV represents as an index of sp^2 content.

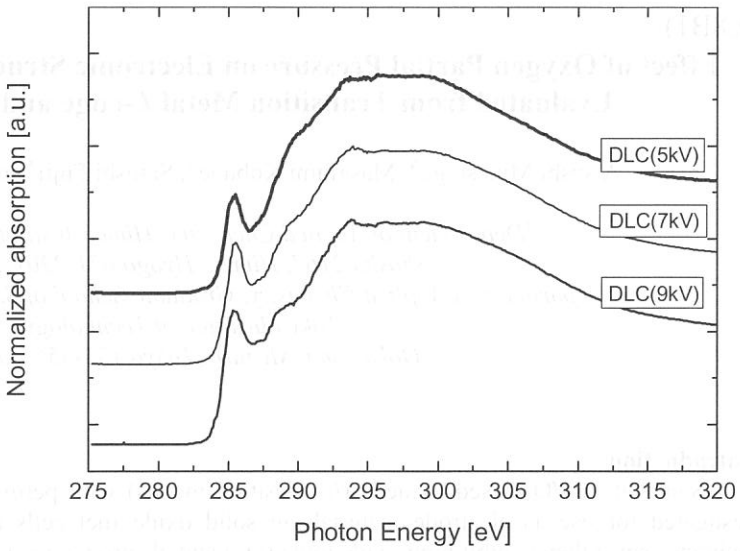

Fig.2 NEXAFS spectra of DLC films deposited with various acceleration voltage.

The established method for the quantitative determination of sp^2 content from EELS technique was applied to the NEXAFS measurements. The sp^2 content was estimated from the integral of the pre-edge peak at 285.3 eV. Further information for the determination of sp^2 content is denoted in the literature [9, 10]. In the fig. 1, the sp^2 contents of the DLC films with the various film thickness were almost same values. This result showed no dependence on the film thickness of the surface structure, since the total electron yield mode of this measurement detected the electrons from the film surface in the depth up to approximately 10 nm. That means homogeneous DLC films could be produced by GCIB assisted deposition under the constant acceleration voltage.

Fig. 2 shows the acceleration voltage dependence of NEXAFS spectra in the DLC films. The DLC films were deposited by varying the GCIB acceleration voltage from 5 to 9 kV with 0.3 μm of film thickness. The intensity of $1s \rightarrow \pi^*$ transitions increases with increasing the GCIB acceleration voltage. The film formed by Ar gas cluster ion beam assisted deposition with 5 kV acceleration voltages has a lowest sp^2 content under this voltage condition.

References

[1] J. Ullmann, Nucl. Instr. and Meth., Phys. Res. B, **127**, 910 (1997).

[2] H. Tsai and D.B. Bogy, J. Vac. Sci. Technol., A **5**, 3287 (1987).

[3] I. Yamada, T. Kitagawa, J. Matsuo and A. Kirkpatrick, Mass. Char. Trans. Inorg. Materials, 957 (2000).

[4] C. Lenardi, P. Piseri, V. Briois, C.E. Bottani, A. Li Bassi and P. Milani, J. Appl. Phys., **85**, 7159 (1999).

[5] A. Hiraya. E. Nakamura, M. Hasumoto, T. Kinoshita, K. Sakai, E. Ishiguro and M. Watanabe, Rev. Sci. Instrum, **66**, 2104 (1995).

[6] P. E. Batson, Phys. Rev. B **48**, 2608 (1993).

[7] M. Jaouen, G. Tourillon, J. Delafond, N. Junqua and G. Hug, Diamond Relat. Mater., **4**, 200 (1995).

[8] J. F. Morar, F. J. Himpsel, G. Hollinger, G. Hughes and J. L. Lordan, Phys. Rev. Lett., **54**, 1960 (1985).

[9] S. D. Berger, D. R. Mc Kenzie and P. J. Martin, Philos. Mag. Lett., **57**, 285 (1988).

[10] P. J. Fallon, V. S. Veerasamy, C. A. Davis, J. Robertson, G. A. J. Amaratunga, W. J. Milne and J. Koskinen, Phys. Rev. B **48**, 4777 (1993).

(BL8B1)

Effect of Oxygen Partial Pressure on Electronic Structure of (La,Sr)(Co,Fe)$O_{3-\delta}$ Evaluated from Transition Metal *L*-edge and O *K*-edge XANES

Atsushi Mineshige[A], Masafumi Kobune[A], Satoshi Fujii[A] and Yoshiharu Uchimoto[B]

[A]*Department of Applied Chemistry, Himeji Institute of Technology*
Shosha 2167, Himeji, Hyogo 671-2201, Japan
[B]*Department of Applied Chemistry, Graduate School of Science and Engineering,*
Tokyo Institute of Technology
Ookayama, Meguro, Tokyo 152-8552, Japan

1. Introduction

Some of La*M*O_3-based oxides (*M*; transition metals) with perovskite-type structure have been widely investigated for use as electrode materials in solid oxide fuel cells (SOFCs) and oxygen semi-permeable membranes since they exhibit high oxide ionic (O^{2-}) and electronic conductivities. Under operating conditions of such devices, the La*M*O_3-based oxides are exposed to gases with various oxygen partial pressures, $P(O_2)$, at elevated temperatures. There are, however, few studies on $P(O_2)$ dependence of their electrical conductivity (σ), although their ionic and electronic conductivities are much affected by a change in $P(O_2)$ because of a deviation in oxygen content from 3. The decrease in the oxygen content from 3 leads to a formation of the oxygen vacancies, paths of an oxide ion transport, and changes the electronic structure, which directly influences their electronic conductivity. In the present study, the change in the electronic structure of Sr-doped La($Co_{0.2}Fe_{0.8}$)O_3 as a function of $P(O_2)$ was studied. In this system, *p*-type electronic conduction is dominant, and σ tends to increase with Sr-doping into La-site or temperature rise (semiconductor-like behavior). The enhancement in σ with Sr content is due to a hole doping. In fact a nominal mean valence of transition metals (*n*) increases to about 3.3 for 40% Sr-doped La($Co_{0.2}Fe_{0.8}$)O_3, while *n* is about 3.0 for undoped sample [1]. The aim of this work is to evaluate a valence of each transition metal, as well as *n*, under several $P(O_2)$ conditions. In addition, the previous study [2] revealed that this system exhibited a curious *p*-type electronic conducting behavior at low $P(O_2)$; *i.e.*, the *p*-type electronic conduction under *n* less than 3. Hence, the relation between the change in its electrical conductivity and that in its electronic structure was also discussed.

2. Experimental

Powders of 40% Sm-doped La($Co_{0.2}Fe_{0.8}$)O_3, $La_{0.6}Sr_{0.4}Co_{0.2}Fe_{0.8}O_3$, which is regarded as one of the best candidate for the cathode material of SOFC, were synthesized from each metal nitrate. It was found that the molar ratio of each metal in the powders thus obtained was desirable by an ICP analysis. Its crystal structure was rhombohedrally distorted with a_r = 5.466 Å, and α_r = 60.33° confirmed by XRD. Then, samples were prepared by re-heating the powders in air at 1273 K, followed by annealing and cooling under various $P(O_2)$ [$10^{-8} \le P(O_2)/\text{atm} \le 0.2$]. The electrical conductivity during cooling was also measured using d.c. 4 probe method under the same $P(O_2)$ conditions. The Co L_{23}-edge, Fe L_{23}-edge and O *K*-edge X-ray Absorption Near Edge Structure (XANES) spectra were measured on the BL-8B1 beam line at UVSOR (Okazaki, Japan) with ring energy of 750 MeV in a mode of total electron yield at room temperature.

3. Results and discussion

Figure 1 shows the Fe *L*-edge XANES of $La_{0.6}Sr_{0.4}Co_{0.2}Fe_{0.8}O_3$ after annealing and cooling in various $P(O_2)$. For comparison, the spectra of $LaFeO_3$ and $SrFeO_3$ are also shown in this figure. A valence of iron is probably 3 in $LaFeO_3$, while iron exhibits two valences of Fe^{3+} and Fe^{4+} in $SrFeO_3$. The absorption at around 708-713 eV is the $2p_{3/2}$ (L_3) edge and that at around 720-725 eV is the $2p_{1/2}$ (L_2) edge. In the spectrum under higher $P(O_2)$, the peak shape resembled that of $SrFeO_3$, exhibiting mixed valences of Fe^{3+} and Fe^{4+}. The sample after cooling in air exhibits about 3.3 of nominal *B*-site mean valence and its oxygen nonstoichiometry (δ in $La_{0.6}Sr_{0.4}Co_{0.2}Fe_{0.8}O_{3-\delta}$) is about 0.05, determined from a weight loss during decomposition [1] and by iodometry [2]. With decreasing $P(O_2)$, no noticeable chemical shifts were observed, but the peak shape in the spectrum slightly changed. In the case of $P(O_2) = 10^{-8}$ atm, the spectrum of the sample and that of $LaFeO_3$ resembled each other. With a decrease in $P(O_2)$, the peak shape changed continuously from $SrFeO_3$-like to $LaFeO_3$-like. This is due to a reduction of Fe valence caused by the formation of oxygen vacancies. The total electrical conductivity (σ), *i.e.*, *p*-type electronic conductivity was about 10^2 and 10^{-1} Scm^{-1}, at room temperature after cooling in air and $P(O_2) = 10^{-4}$, respectively. Hence, it is found that the change in σ is well corresponded to the change in a concentration of charge carriers (electronic hole). It should be, however, noted that the Fe ions have mixed valences of Fe^{3+} and Fe^{4+} rather than Fe^{3+} alone, even in the strongly reducing

condition of $P(O_2) = 10^{-8}$ atm (Fig. 1). This indicates that the charge carriers still exist at that condition.

Figure 2 shows the Co *L*-edge XANES of the same samples. The spectra of $LaCoO_3$ and CoO are also shown in this figure for comparison. The absorption at around 775-782 eV is the $2p_{3/2}$ (L_3) edge and that at around 790-797 eV is the $2p_{1/2}$ (L_2) edge. The spectral features near 783 and 798 eV under the lower $P(O_2)$ conditions were unknown at present. The peak of $LaCoO_3$, exhibiting a valence of ca. 3 appeared at 779.22 eV, whereas that of CoO, exhibiting a valence of ca. 2 appeared at 776.92 eV. This figure shows that the mixed valences of cobalt in the samples changed from Co^{3+}-Co^{4+} to Co^{2+}-Co^{3+} with decreasing $P(O_2)$. Our previous work [2] revealed that *p*-type electronic conduction appeared in the $P(O_2)$ range [$10^{-11} \leq P(O_2)$/atm ≤ 1 at 1273 K], while δ is equal to 0.28 (2.84 of nominal *B*-site mean valence) at 10^{-8} atm of $P(O_2)$ at the same temperature. Hence it is suggested that the appearance of Co^{2+} enabled the *p*-type electronic conduction to appear in the wide range of $P(O_2)$ even if the mean valence of *M* is less than 3. While the formation of Co^{2+} may not be preferable in view of the stability of the structure in (La,Sr)CoO_3 system, in the case of (La,Sr)$Co_{0.2}Fe_{0.8}O_3$, *B*-site sublattice, consisting mainly of Fe ions may stabilize Co^{2+} ions.

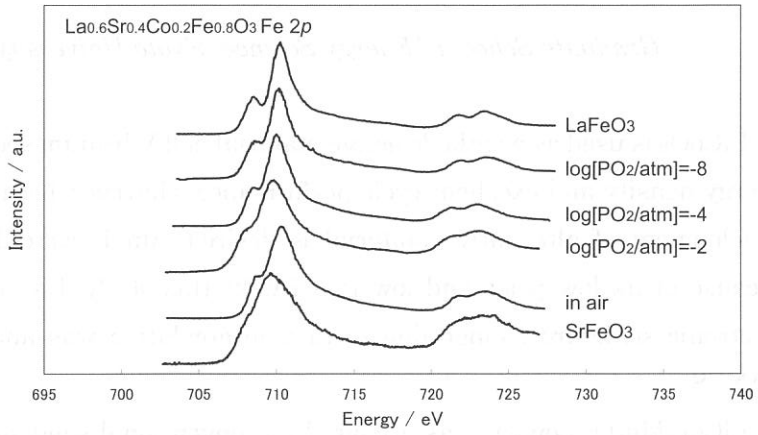

Fig. 1. Fe2*p* X-ray absorption spectra of samples.

Figure 3 shows the O *K*-edge XANES of the samples. The peak near 528 eV is attributed to the band derived from the mixing of the transition metal 3*d* states with O 2*p* states. The prepeak near 527 eV is attributed to the hole state, containing O 2*p* character caused by Sr-substitution. With decrease in $P(O_2)$, the prepeak disappeared along with the oxygen vacancy formation. Oxygen atoms containing this hole state with O 2*p* character may be transformed easily into neutral oxygen molecules under low $P(O_2)$, leaving the oxygen vacancies at the lattice. In conclusion, the role of each element to the electric conducting behavior was revealed by XANES studies on $La_{0.6}Sr_{0.4}Co_{0.2}Fe_{0.8}O_{3-\delta}$. In the further work, a quantitative observation regarding the hole concentration at each position has to be done.

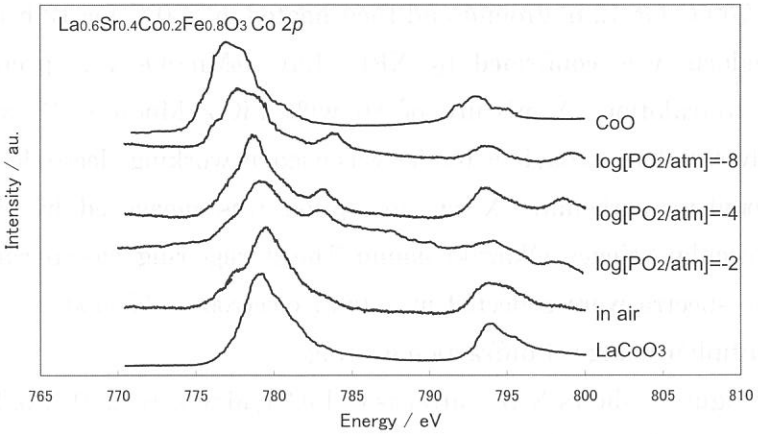

Fig. 2. Co2*p* X-ray absorption spectra of samples.

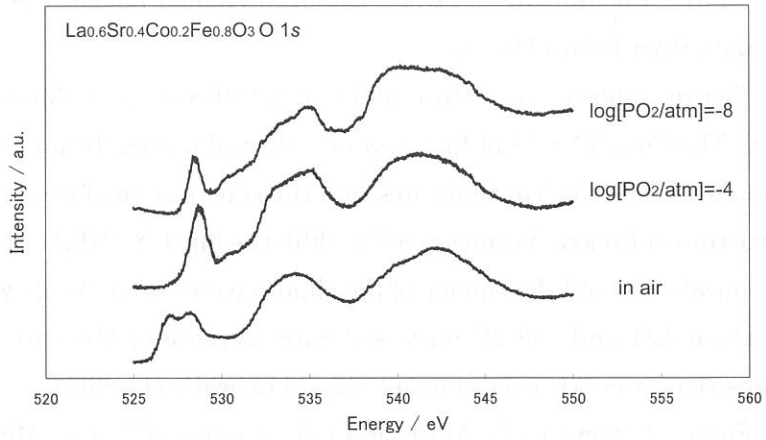

Fig. 3. O1*s* X-ray absorption spectra of samples.

References

[1] L-W. Tai, M. M. Nasrallah and H. U. Anderson, *J. Solid State Chem.*, **118,** 117 (1995).

[2] A. Mineshige, J. Izutsu, M. Nakamura, K. Nigaki, M. Kobune, S. Fujii, M. Inaba, Z. Ogumi and T. Yao, *Electrochemistry,* **68,** 515 (2000).

(BL-8B1)

Electronic Structure Change by Li deintercalation in $Li_xCo_{1-y}Mn_yO_2$ from Co-L, Mn-L and O-K XANES

Naoshi OZAWA, Yoshiharu UCHIMOTO, Hiroshi SAWADA and Takeshi YAO

Graduate School of Energy Science, Kyoto University, Kyoto, 606-8501 Japan

$LiCoO_2$ is used as a cathode active material of 4 V lithium secondary battery, because of its high energy density and excellent cycle performance. However, because Co is expensiveness and toxic, development of alternative material is desired. Mn is candidates for the alternative material because of its low price and low toxicity. In this study, $LiCo_{1-y}Mn_yO_2$ was synthesized and the electronic structure change due to Li deintercalation was analyzed from Co-L, Mn-L and O-K XANES.

$LiCo_{1-y}Mn_yO_2$ powder was prepared by conventional solid state reaction starting with lithium hydroxide (Wako Chemical Co. Inc., 99.9 %), cobalt hydroxide (Wako Chemical Co. Inc., 99.9 %), and manganese hydroxide (Wako Chemical Co. Inc., 99.9 %). Mixtures of low material was heated at 700°C for 12 h, ground and then heated at 800°C for 12 h in air. The crystal structure of the products was confirmed by XRD. $Li_xCo_{0.9}Mn_{0.1}O_2$ was prepared by electrochemical lithium deintercalation. A mixture of 80 wt% $LiCo_{0.9}Mn_{0.1}O_2$, 15 wt% acetylene black, and 5 wt% polytetrafluoropropylene binder was used as working electrode. The electrolyte was 1 M $LiClO_4$ in propylene carbonate. X-ray absorption was measured by BL-8B1 at UVSOR, Institute for Molecular Science, Okazaki, Japan. The storage ring was operating at electron energy of 750 MeV. The spectra were collected in a total electron yield mode at room temperature by an electron multiplier using G1 diffraction grating.

Figure 1 shows XRD patterns of $LiCo_{1-y}Mn_yO_2$ (y=0, 0.1, 0.2). The patterns were indexed to a rhombohedral lattice and $R\bar{3}m$ space group. For $LiCo_{0.8}Mn_{0.2}O_2$, tiny unknown peak was observed at about 37 °.

Figure 2 shows the electrode potential change during the electrochemical deintercalation of lithium from $LiCo_{0.9}Mn_{0.1}O_2$.

Figure 3 shows Co-L, Mn-L and O-K XANES of $LiCo_{1-y}Mn_yO_2$ (y=0, 0.1, 0.2). As shown in Fig. 3(a), The Co-L XANES of $LiCo_{1-y}Mn_yO_2$ showed no significant chemical shift and the change of the shapes were small. This indicates that the substitution of Co with Mn does not affect the electronic structure of Co ion. As shown in Fig. 3(b), the Mn-L XANES of $LiCo_{1-y}Mn_yO_2$ showed no significant chemical shift and the change of the shapes were small. As shown in Fig. 3(c), the peak intensities at about 531 and 533 eV increased with increase of Mn content. These peaks are attributed to transition from O1s orbital to O2p-Mn3d hybridized orbital[1].

Figure 4 shows Co-L, Mn-L and O-K XANES of $Li_xCo_{0.9}Mn_{0.1}O_2$ (x=0.2, 0.4, 0.6, 0.8, 1.0). As shown in Fig. 4(a), the Co-L XANES of $Li_xCo_{0.9}Mn_{0.1}O_2$ showed no remarkable chemical shift and

the change of the shapes were small. This indicates that the valence of Co ion was almost unchanged by deintercalation of Li from $LiCo_{0.9}Mn_{0.1}O_2$. As shown in Fig. 4(b), the Mn-L XANES of $Li_xCo_{0.9}Mn_{0.1}O_2$ showed no significant chemical shift and the change of the shapes were small. This indicates that the valence of Mn ion was almost unchanged by intercalation of Li from $LiCo_{0.9}Mn_{0.1}O_2$. As shown in Fig. 4(c), by extracting lithium from $LiCo_{0.9}Mn_{0.1}O_2$, the peak shape at about 529 to 533 eV changed and a new shoulder was observed at about 527 eV. This indicates that oxidation by lithium deintercalation is mainly related to the electrons in O2p orbital.

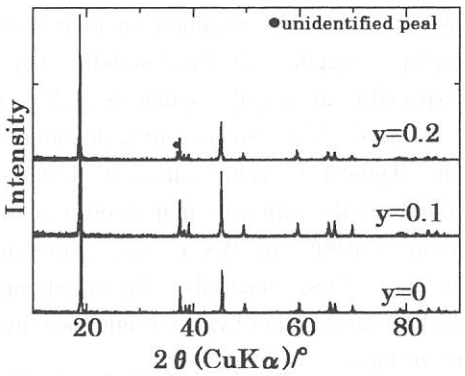

Fig.1 XRD patterns of $LiCo_{1-y}Mn_yO_2$ (y=0, 0.1, 0.2).

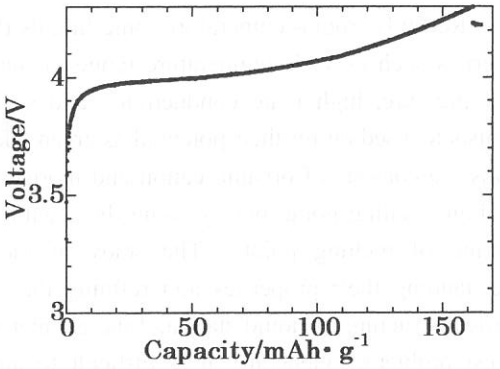

Fig.2 Electrode potential change of $LiCo_{0.9}Mn_{0.1}O_2$ electrode during the charge process.

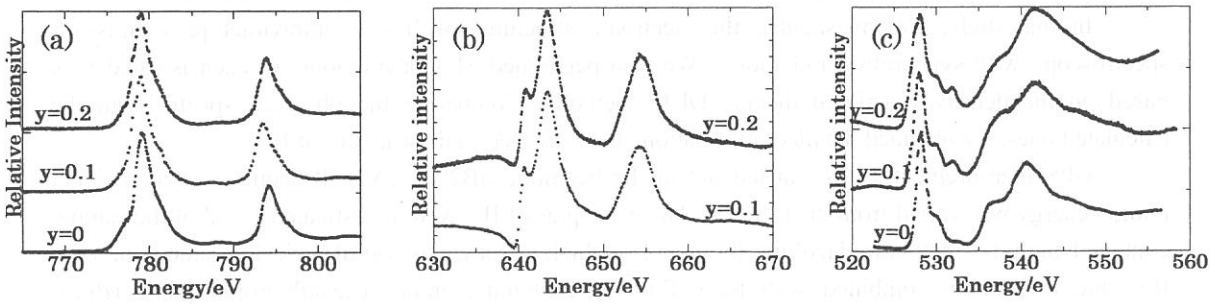

Fig.3 (a) Mn-L, (b) Co-L and (c) O-K XANES of $LiCo_{1-y}Mn_yO_2$ (x=0, 0.1, 0.2).

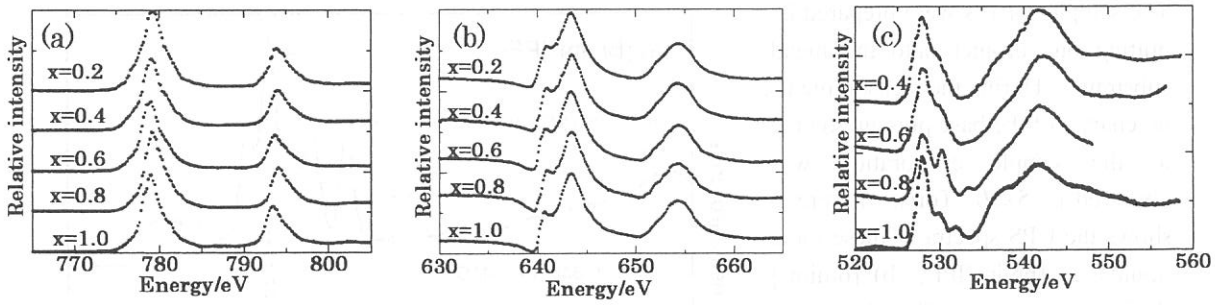

Fig.4 (a) Mn-L, (b) Co-L and (c) O-K XANES of $Li_xCo_{0.9}Mn_1O_2$ (x=0.2, 0.4, 0.6, 0.8, 1.0).

Reference

1) M.Abbate et. al., *Phys. Rev. B*, 46, 4551 (1992).

(BL8B2)

Electronic Structure of Ionic Liquids Studied by UV Photoemission

D. Yoshimura,[a,b] T. Yokoyama,[c] T. Nishi,[c] H. Ishii,[c] K. Seki,[a] R. Ozawa,[d] and H. Hamaguchi[d]

a) Research Center for Materials Science, Nagoya University, Chikusa-ku, Nagoya 464-8602, Japan

b) Institute for Molecular Science, Myodaiji, Okazaki 444-8585, Japan

c) Department of Chemistry, Graduate School of Science, Nagoya University, Chikusa-ku Nagoya 464-8602, Japan

d) Department of Chemistry, Graduate School of Science, The University of Tokyo, Hongo Tokyo 113-0033, Japan

Recently, room-temperature ionic liquids (ILs) have attracted much attention for their excellent properties such as wide temperature range of the liquid phase, excellent chemical stability, very low vapor pressure, high ionic conductivity, and so on. Especially, among the synthesis and catalysis chemists focused on for their potential as green "designer solvents".[1,2] Such room-temperature ionic liquids are consists of organic cation and inorganic anion. Typical inorganic salts (*e.g.* Na^+Cl^-) have very high melting point, but by using the organic compounds as the cation brought about remarkable lowering of melting point. The study of the electronic structure of ILs is very important to understanding their properties and refining the performance of these materials. To investigate the electrical structure of liquid state and the geometrical structures at the liquid/vacuum interface are also interest problem. Generally it is difficult to apply the surface scientific techniques to the liquid state sample. But the nature of very low vapor pressure of ILs enables us the measurement in ultra-high vacuum (UHV) condition. However, there have been few studies that directly observed the electronic structure of ILs.

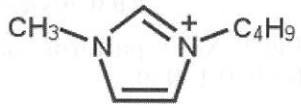

Fig.1 molecular structure of $bmim^+$

In this study, we investigated the electronic structures of ILs by ultraviolet photoemission spectroscopy with synchrotron radiation. We also performed MO calculations for each isolated ions based on the density functional theory (DFT) method. Comparing the observed spectra with the calculated ones, we obtained detailed information about the electronic structure of ILs.

UPS measurements were carried out at the beamline 8B2 of UVSOR facility. The incident photon energy was varied from 20-120eV. Three samples of ILs were investigated. All of the sample contain 1-buthyl-3-methylimidazolium ($bmim^+$) [3] which is known as one of typical organic cation for ILs, and this cation combined with three fluorine containing anions (hexafluorophosphate (PF_6^-), tetrafluoroboronate (BF_4^-), bis(trifluoromethanesulfonyl)imide ($CF_3(SO_2)_2N^-$; Tf_2N^-). All of these ILs are in the liquid phase at room temperature. In Figure 1, we show the molecular structure of $bmim^+$. The samples of ILs were prepared by putting one droplet onto the metal substrate. During the measurements, no change of the base pressure owing to the sample evaporation was observed (< 5×10^{-10}Torr). Figure 2 shows the UPS spectra of these ionic liquids; a) $[bmim^+]PF_6^-$, b) $[bmim^+]BF_4^-$, c) $[bmim^+]CF_3(SO_2)_2N^-$. The incident photon energies of the spectra were 80eV for Fig 2a and 60eV for Figs. 2b and 2c. The abscissa of the spectra is the binding energy relative to the vacuum level.

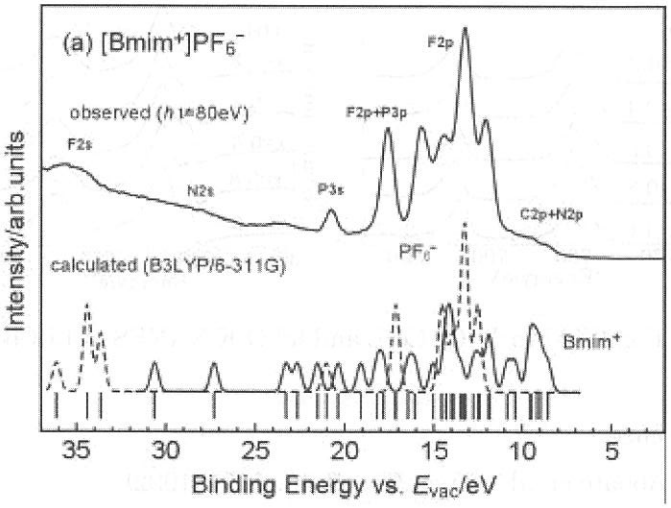

Fig. 2(a) Observed and calculated spectra of $[bmim^+]PF_6^-$.

We also performed MO calculations for each isolated ions based on the density functional theory (DFT). The calculations were performed by GAUSSIAN98 with B3LYP parameters and 6-311G basis set. Below the observed spectra in Figs. 2, we show the calculated density of states (DOS) by convoluting each calculated states with a Gaussian function (FWHM = 0.5eV) under the assumption that the emission intensities from each orbital were the same. Each of the calculated DOS for the isolated ions was shifted in the energy scale for better correspondence with the observed spectra. The direction and the amount of the shifts were shown in Table 1, together with the experimentally obtained values of ionization potential (IP) of these ILs from the another UPS measurements.[2] Comparing the observed spectra with the simulated ones, there was fairly good agreement with each other. Therefore, it is concluded that the top of the valence band is derived from the HOMO of the $bmim^+$. We can assign the another peaks of ILs' spectra based on the calculation as shown in Figs. 2. In these figures, we can see the trend that the orbital energies of the cation ($bmim^+$) were unstabilized, and those of anions were stabilized against the predicted value by the calculations. Before the shift in the energy scale, the calculated HOMO of $bmim^+$ lay deeper than its counter anions. This inversion of the top of the valence states can be explained by the effect of Mudelung energy. Lastly, we mention that the molecular orientation of $bmim^+$ in the liquid phase from our recent results of NEXAFS measurements.[2] Next, we will try to obtain more detailed information about molecular orientation from ARUPS measurements.

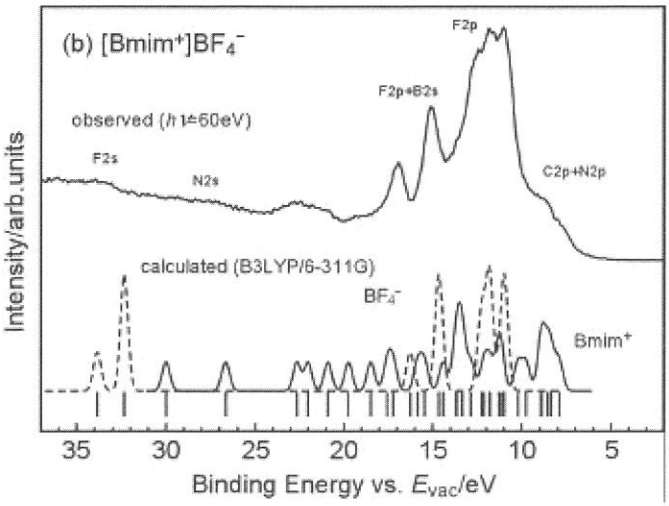

Fig. 2(b) Observed and calculated spectra of $[bmim^+]BF_4^-$.

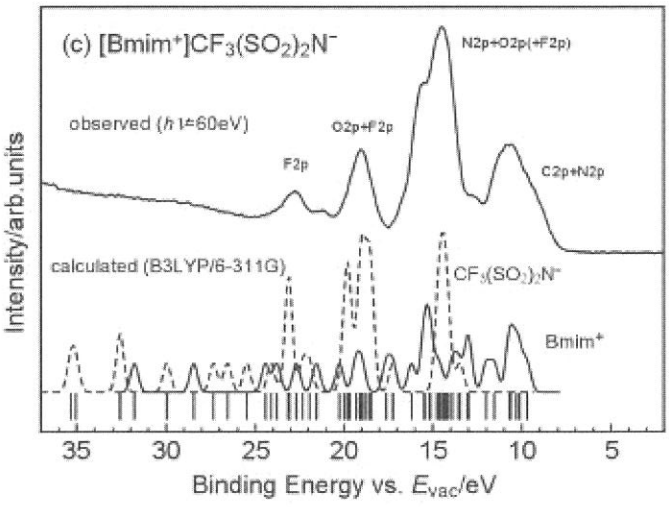

Fig. 2(c) Observed and calculated spectra of $[bmim^+]CF_3(SO_2)_2N^-$.

	I_{th}	Shifts in energy scale	
		Cation	Anion
$[bmim^+]PF_6^-$	7.85	-3.1	+6.9
$[bmim^+]BF_4^-$	6.68	-2.1	+9.3
$[bmim^+]Tf_2N^-$	7.82	-3.9	+6.8

(in eV)

Table 1. Ionization potential and the energy shifts.

References

[1] T. Welton, Chem Rev. **99** 2071 (1999).

[2] P. Wassescheid and W. Keim, Angew. Chem. Innt. Ed., **39** 3772 (2000).

[3] P.A.Z. Suarez, S. Einloft, J.E.L. Dullius, R.F. de Souza and J. Dupont, J. Chim. Phys. **95** 1626 (1998).

[4] T. Nishi, to be published.